

Fakultät für Physik und Astronomie
Ruprecht-Karls-Universität Heidelberg

Masterarbeit

im Studiengang Physik

vorgelegt von: Kolja Reuter

aus (Geburtsort): Seesen

geboren am: 23.08.2001

Department of Physics and Astronomy
University of Heidelberg

Master Thesis

in Physics

submitted by: Kolja Reuter

born in: Seesen

year of submission: 2025

under the supervision of: Prof. Dr. Dominika Wylezalek

carried out at: Astronomische Recheninstitut Heidelberg

“The evolution of the universe can be likened to a display of fireworks that has just ended: some few red wisps, ashes, and smoke. Standing on a well-chilled cinder, we see the fading of the suns and try to recall the vanished brilliance of the origin of the worlds.”

Lemaître in 2001

Abstract

Active galactic nuclei (AGN) feedback plays a crucial role in galaxy evolution, yet the persistence of AGN-driven outflows after the central engine fades remains poorly constrained observationally. This thesis presents a systematic search for fossil outflows in the KMOS^{3D} survey, comprising 739 galaxies at $0.6 < z < 2.7$. We developed an automated emission-line fitting pipeline employing single and double Gaussian models for the $H\alpha+[N II]$ complex, combined with Voronoi binning to achieve uniform signal-to-noise across the whole galaxy. Using the non-parametric W_{80} velocity width and WHAN diagnostic classifications, we identify eight fossil outflow candidates exhibiting broadened emission-line profiles ($W_{80} > 300 \text{ km s}^{-1}$), lopsided kinematic morphologies, and spatial detachment from the nucleus—signatures predicted by hydrodynamical simulations—while lacking current AGN activity in the Milliquas catalogue and SIMBAD. Our detection rate of $\sim 1.4\%$ is consistent with theoretical predictions that fossil outflows may be several times more common than actively-driven ones. These candidates represent promising targets for follow-up observations to confirm the fossil outflow interpretation and constrain the duty cycle of AGN feedback at cosmic noon.

Kurzfassung

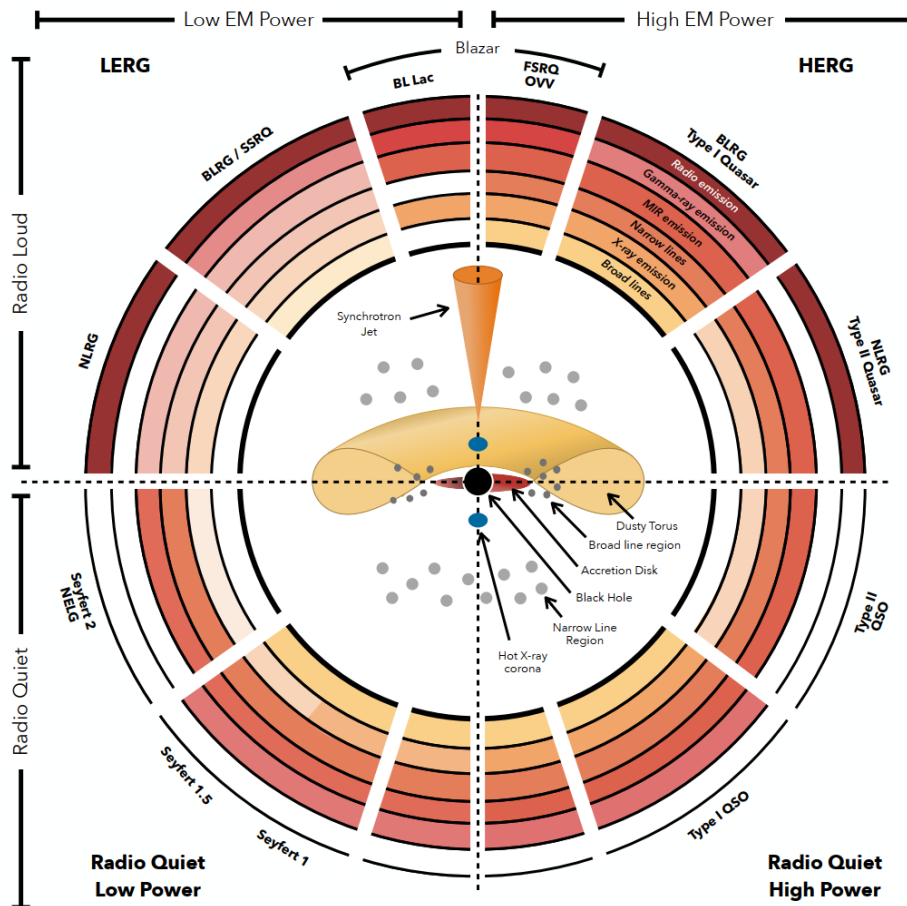
Die Rückkopplung aktiver Galaxienkerne (AGN) spielt eine entscheidende Rolle in der Entwicklung von Galaxien, doch die Persistenz von AGN-getriebenen Ausflüssen nach dem Erlöschen des zentralen Motors ist beobachtungsmäßig nach wie vor schlecht eingeschränkt. Diese Arbeit präsentiert eine systematische Suche nach fossilen Ausflüssen in der KMOS^{3D}-Studie, die 739 Galaxien bei $0,6 < z < 2,7$ umfasst. Wir haben eine automatisierte Pipeline zur Anpassung von Emissionslinien entwickelt, die einfache und doppelte Gauß-Modelle für den $H\alpha+[N II]$ -Komplex verwendet, kombiniert mit Voronoi-Binning, um ein einheitliches Signal-Rausch-Verhältnis über die komplette Galaxie zu erreichen. Unter Verwendung der nichtparametrischen W_{80} -Breite und der WHAN-Diagnoseklassifikationen identifizieren wir acht Kandidaten für fossile Ausflüsse, die verbreiterte Emissionslinienprofile ($W_{80} > 300 \text{ km s}^{-1}$), asymmetrische kinematische Morphologien und räumliche Ablösung vom Kern aufweisen – Signaturen, die durch hydrodynamische Simulationen vorhergesagt werden –, während sie im Milliquas-Katalog und in SIMBAD keine aktuelle AGN-Aktivität aufweisen. Unsere Erkennungsrate von $\sim 1,4\%$ stimmt mit theoretischen Vorhersagen überein, dass fossile Ausflüsse möglicherweise um ein Vielfaches häufiger vorkommen als aktiv angetriebene. Diese Kandidaten sind vielversprechende Ziele für Folgebeobachtungen, um die Interpretation als fossile Ausflüsse zu bestätigen und den Arbeitszyklus der AGN-Rückkopplung zur kosmischen Hochzeit einzugrenzen.

1 Introduction: AGN Feedback and Galaxy Evolution

active galactic nuclei (AGN) are highly energetic phenomena where the accretion disk of the supermassive black hole (SMBH) at the galactic center outshines and dominates the rest of the host galaxy (Netzer, 2013; Schneider, 2015). In modern astrophysics, the AGN is understood as a transient phase in galaxy evolution; current models suggest that every galaxy eventually undergoes an "active phase" during which its central SMBH experiences significant mass growth via its accretion disk (Hickox & Alexander, 2018). This hypothesis—alongside the premise that virtually every massive galaxy hosts a central SMBH (**Kormendy:SMBH**)—is widely accepted, though definitive proof remains a challenge in observational astronomy (Volonteri, 2010).

In the following sections, we describe the general structure of AGNs before discussing their coevolution with host galaxies (Kormendy & Ho, 2013). For the scope of this thesis, we do not differentiate AGNs into their various subclassifications (Urry & Padovani, 1995), as such distinctions are not central to the current analysis and would require a more exhaustive treatment than is feasible here.

1.1 The structure of AGN



J. E. Thorne

Figure 1: Unified Model of AGN-classification by Thorne (2021).

AGNs exhibit unique structural properties that distinguish them from standard galaxies classified via the Hubble scheme (Hubble, 1926). Their radiation displays high temporal variability, a spectrum spanning from radio to gamma rays, and prominent emission lines (Beckmann & Shrader, 2012). Unlike stellar populations, AGN emission is predominantly non-thermal (Schneider, 2015). These active nuclei are found in approximately 10% of all galaxies (Padovani et al., 2017). While the fundamental structure is similar across most AGNs, the observed variability and measured intensities are strongly dependent on the observer’s viewing angle relative to the accretion disk’s rotation axis (Schneider, 2015; Urry & Padovani, 1995).

Typically, AGN light is polarized due to scattering by ordered, rotating dust (Antonucci, 1993). AGNs are further classified as radio-loud or radio-quiet, depending on the contribution of emission from jets and lobes formed by the disk (Kellermann et al., 1989). As illustrated in @todo, these objects are powered by geometrically-thin accretion disks around SMBHs with masses of typically $10^6\text{--}10^9 M_\odot$ (Shakura & Sunyaev, 1973). The basic structure consists of several components: the central SMBH, the accretion disk, the broad line region (BLR), and the narrow line region (NLR), all surrounded by a dusty torus (Netzer, 2015). The accretion disk, which is hotter and denser than the interstellar medium, emits intense UV and X-ray radiation (Cantiello et al., 2021). When the black hole’s spin and the disk’s magnetic field are aligned, powerful jets can be produced (Blandford & Znajek, 1977; Schneider, 2015).

The BLR consists of gas clouds in highly elliptical orbits within light-days of the SMBH (Peterson, 2006). Intense radiation and high kinetic energy ionize this gas, resulting in broad emission lines (Netzer, 2013). Conversely, the NLR is situated further out (hundreds of parsecs), where the gas is excited by radiation from the disk and BLR (Osterbrock & Ferland, 2006). While BLRs are confined to sub-pc scales with velocities of $10^3\text{--}10^4$ km/s, NLRs can span kpc scales, comparable to the galaxy bulge—with velocities of $10^2\text{--}10^3$ km/s (Stockton & MacKenty, 1984).

Further out the Extended Narrow Line Region (ENLR) is excited by AGN radiation pressure rather than star formation, a key distinction from the Extended Emission Line Region (EELR) (Tadhunter et al., 1987). Identifying ENLRs in Seyfert galaxies, quasars, and radio galaxies provides a tracer for past AGN activity (Zubovas et al., 2022). The dusty torus plays a critical role in the Unified Model, obscuring the nucleus from certain angles to create the distinction between Type 1 and Type 2 AGNs (Antonucci, 1993). Furthermore, many AGNs possess a relativistic jet and an X-ray corona, both of which are central to understanding feedback mechanisms (Fabian, 2012).

1.2 AGN feedback

This section explores the large-scale effects of an active SMBH on galaxy evolution, collectively known as AGN feedback (Fabian, 2012). This feedback encompasses the influence of high-energy radiation and matter outflows on the host galaxy’s molecular gas density and temperature (Silk1998). The plausibility of such a small nucleus influencing a whole galaxy is often illustrated by the "coin-on-the-moon" analogy, where the SMBH acts as a 1-cent coin affecting the entire lunar body (A. King & Pounds, 2015).

Indicators of this coevolution include the $M\text{--}\sigma$ relation—an empirical correlation between stellar

velocity dispersion σ and SMBH mass M (**Fabian:AGN2012**):

$$\frac{M_{BH}}{10^8 M_\odot} = 3.1 \cdot \left(\frac{\sigma}{200 \frac{\text{km}}{\text{s}}} \right)^4. \quad (1)$$

This relationship implies a feedback loop that maintains the link between the black hole and the bulge despite mergers and accretion (Ferrarese & Merritt, 2000; Gebhardt et al., 2000). (Silk & Rees, 1998) proposed that SMBHs form through gas cloud collapse, creating winds that regulate the bulge's star formation. Comparing the accretion energy $E_{BH} = 0.1 M_{BH} c^2$ with the galaxy's binding energy $E_{gal.} = M_{gal.} \sigma^2$ (given $M_{BH} \approx 10^{-3} M_{gal.}$), we find:

$$\frac{E_{BH}}{E_{gal.}} \approx 1 \cdot 10^{-4} \left(\frac{c}{\sigma} \right)^2. \quad (2)$$

For galaxies where $\sigma < 400$ km/s, this results in:

$$\frac{E_{BH}}{E_{gal.}} > 80 \quad (3)$$

This demonstrates that SMBH growth releases enough energy to profoundly affect the host galaxy if even a small fraction is coupled to the gas (Fabian, 2012). Feedback is classified as mechanical or radiative (Harrison et al., 2018). While radio jets heat the intergalactic medium, they are present in only a small fraction of AGNs (Mahatma et al., 2018). Radiative feedback is characterized by kinematic signatures such as blue-shifted velocity profiles and broad forbidden emission lines (> 1000 km/s), which suggest a strongly ionized Interstellar Medium (ISM) (Genzel et al., 2014; Schneider, 2015). Finally, the simultaneous peak of quasar activity and star formation at redshift $z = 2$ strongly suggests their coevolution (**Madau:1996**; Madau & Dickinson, 2014).

1.3 AGN Influence on the $H\alpha$ Emission Line

At the most fundamental level, emission lines in astronomy originate from quantum mechanical transitions within atoms or molecules. When electrons in an atom or molecule drop from a higher energy level (excited state) to a lower one, they release the energy difference as a photon of light. Because these energy levels are quantized and unique to each element or molecule, the emitted light appears at specific, characteristic wavelengths, allowing astronomers to determine the chemical composition of nebulae and galaxies. However, these lines are rarely observed as infinitely thin spikes at a single wavelength. Instead, they exhibit measurable widths and complex shapes, or profiles, where the natural line width is determined by the Heisenberg uncertainty principle, relating the finite lifetime of an excited state to an uncertainty in the energy and frequency of the emitted photon. In astronomical contexts, external environmental factors usually dominate this natural width, reshaping the line profiles significantly. The observed shapes result from a convolution of intrinsic atomic physics and macroscopic kinematic effects. One primary cause of line broadening is the Doppler effect caused by the motion of the emitters. In any gas, particles move randomly due to temperature; this thermal motion causes slight redshifts and blueshifts for individual emitters, resulting in a Gaussian broadening of the spectral line. In the broad line region (BLR) of active galactic nuclei (AGN), high-velocity turbulent motion is a dominant factor, often producing Lorentzian profiles rather than Gaussian ones, with turbulent

velocities in the BLR ranging from for up to for high-ionization lines like .

When gas rotates around a central mass such as a black hole, the side moving towards the observer is blueshifted, while the side moving away is redshifted. This rotational broadening can reach velocities up to and, depending on inclination, may appear as double-peaked profiles, though local turbulence often smooths these into a single broad peak. In magnetized plasmas, external fields alter line shapes via Stark broadening, caused by electric microfields, and the Zeeman effect, where magnetic fields split atomic levels. Furthermore, atoms moving through a strong magnetic field (Tesla) experience an induced electric field leading to the Motional Stark Effect (MSE), which significantly distorts profiles. In the context of galaxy evolution, diagnostic line shapes arise from non-gravitational kinematics like outflows. A hallmark of galactic outflows is an asymmetric line profile featuring a prominent "blue wing," occurring when gas expands outward from the nucleus and the approaching gas is blueshifted while the receding gas is obscured by dust. Spectra are often modeled by decomposing lines into narrow components (λ), tracing the host galaxy's gravitational potential, and broad components (λ), which signify AGN-driven feedback. In the X-ray and UV regimes, these outflows manifest as P-Cygni profiles, consisting of a blueshifted absorption trough followed by an emission peak, characteristic of Ultra-Fast Outflows (**ufo!**s (**ufo!**s)).

In optical and near-infrared spectroscopy, the emission line (λ) is a primary diagnostic for star formation and AGN activity (Kennicutt, 1998). AGNs significantly alter the profile via broadening, where Type 1 AGNs show broad components from the BLR exceeding FWHM of (Osterbrock & Ferland, 2006), and via AGN-driven winds that create blue-shifted wings indicating ionized gas outflows (Genzel et al., 2014). To quantify this feedback, the parameter is defined as the velocity width encompassing 80% of the line flux:

$$W_{80} = v_{90} - v_{10} \tag{4}$$

where and are the 10th and 90th percentiles of the profile (Zakamska & Greene, 2014). For Gaussian profiles, ; values indicate powerful AGN-driven outflows (Förster Schreiber et al., 2019; Harrison et al., 2014).

Galaxy-wide outflows are fundamental regulators of evolution (A. King & Pounds, 2015), yet the lack of correlation between instantaneous AGN luminosity and outflow properties suggests the active phase is shorter than the outflow's duration (Zubovas, 2018). Fossil outflows are gas flows that persist due to inertia and thermal pressure after the AGN has faded (A. R. King et al., 2011). As the wind shocks the surrounding gas, it heats up to K, and the shocked interstellar medium (ISM) expands adiabatically with kinetic power – (Zubovas et al., 2022). Using *Gadget-3* hydrodynamical Smoothed Particle Hydrodynamics (SPH) simulations, Zubovas et al. (2022) demonstrated that fossil outflows form when:

$$\frac{L_{\text{AGN}}}{L_{\text{Edd}}} \gtrsim 7f_g \tag{5}$$

The expansion is driven by the high pressure of the shocked wind:

$$P_w \simeq 5 \times 10^{-10} \left(\frac{\dot{M} * w}{2.2, M * \odot, \text{yr}^{-1}} \right) R^{-2} * \text{kpc} \left(\frac{T * \text{sh}}{10^{10}, \text{K}} \right), \text{erg, cm}^{-3} \tag{6}$$

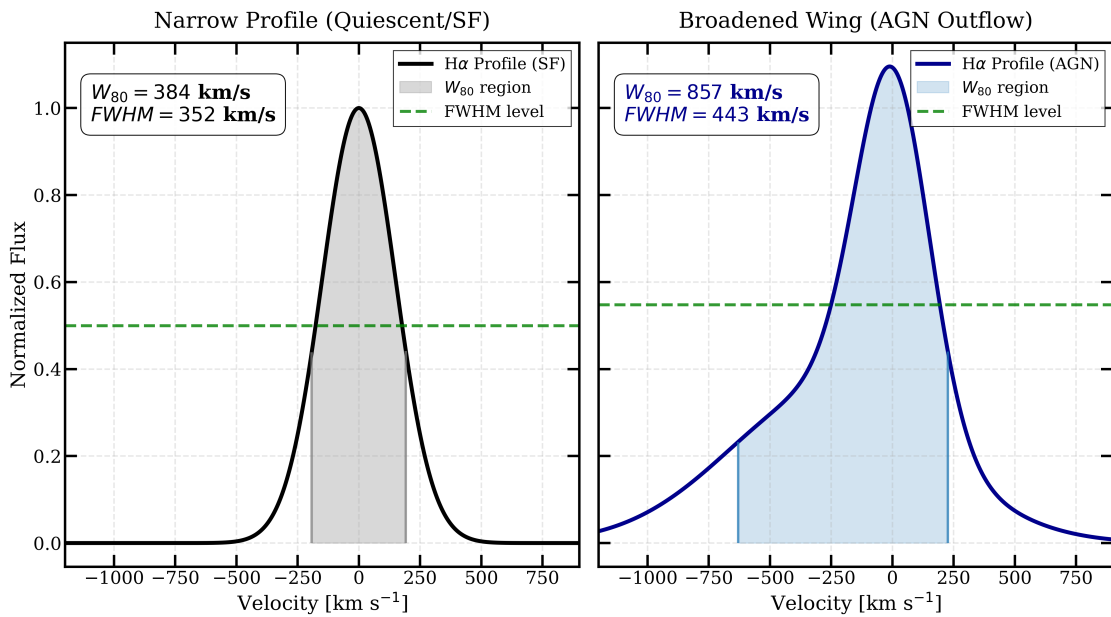


Figure 2: Comparison of the parameter for a symmetric star-forming galaxy (left) and a galaxy with an AGN-driven outflow (right) (Harrison et al., 2014). The shaded area represents the flux interval.

which exceeds the ISM pressure by two orders of magnitude (Zubovas & King, 2012). Fossil outflows cool rapidly once the radiation field vanishes, causing the luminosity to plummet and potentially leading to the misclassification of powerful outflows. These systems are characterized by a dominant molecular phase relative to the ionized phase (λ) and spatial detachment from the nucleus, often appearing as "holes" in Integral Field Unit (Integral Field Unit (IFU)) maps (Harrison et al., 2014; Zubovas et al., 2022). Furthermore, fossil outflows can trigger in-situ star formation in outer regions where young stars maintain radial trajectories while gas is decelerated. Zubovas et al. (2022) concluded that fossil outflows may be 2 to 10 times more common than active ones in the local Universe, exhibiting higher lopsidedness and higher mass flow rates for a given velocity due to their larger spatial extent.

1.4 Line Diagnostic: The diagnostic diagram based on the equivalent width of H α and the [N II] λ 6584/H α ratio (WHAN)-Diagram

The WHAN diagram, introduced by Cid Fernandes et al. (2010) and refined in Cid Fernandes et al. (2011), provides a powerful diagnostic tool for classifying emission-line galaxies using only two spectral features: the equivalent width of the H α emission line ($W_{H\alpha}$) and the [N II] λ 6584/H α flux ratio. This two-dimensional classification scheme offers several advantages over traditional diagnostic diagrams while maintaining a solid theoretical foundation rooted in photoionization physics.

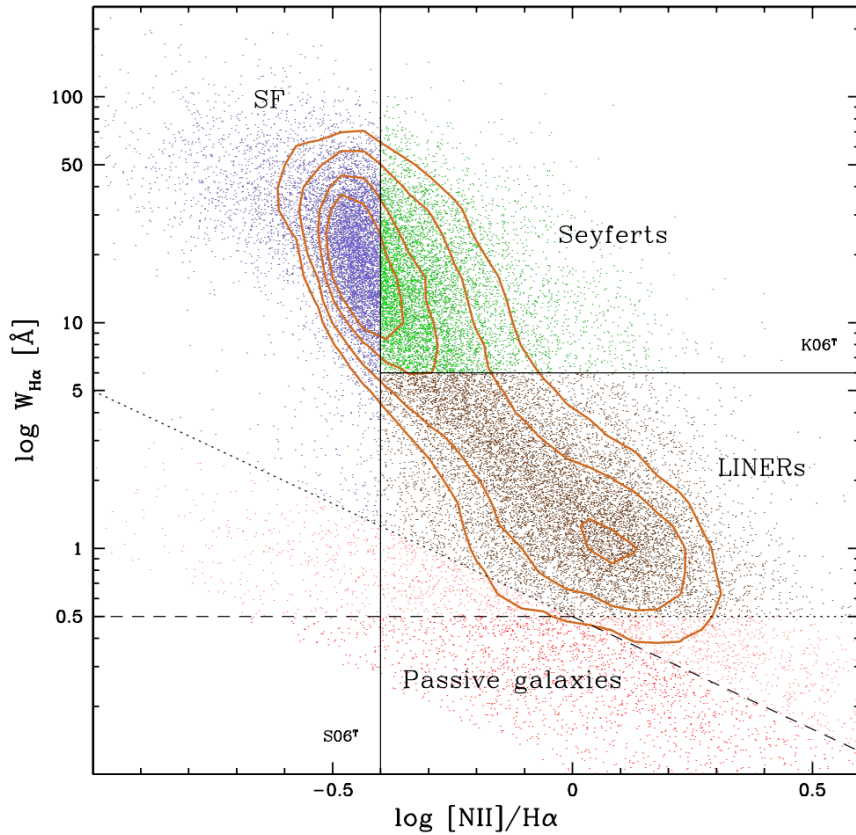


Figure 3: The WHAN diagram showing the classification of emission-line galaxies based on equivalent width of $H\alpha$ ($W_{H\alpha}$) versus the emission-line ratio $[N II]/H\alpha$. Different galaxy populations are separated by the indicated demarcation lines: star-forming galaxies (SF, blue), Seyferts (green), LINERs (brown), and passive galaxies (red). The line labelled $S06^T$ represents the transposition of the Stasińska et al. (2006) classification, while the horizontal line at $W_{H\alpha} = 6 \text{ \AA}$, labelled $K06^T$, corresponds to the transposed Seyfert/LINER division from Kewley et al. (2006). Orange contours, as well as the coloured dots trace galaxies in two different samples from the SDSS sample, adapted from Cid Fernandes et al. (2011).

1.4.1 Advantages over the diagnostic based on the ratio of a high ionization line to a low one, named after Baldwin, Phillips and Terlevich (BPT) Diagram

The BPT diagram (Baldwin et al., 1981) has long served as the primary tool for distinguishing ionization mechanisms in galaxies. However, the classical BPT approach requires reliable measurements of four emission lines—[O III] λ 5007, H β , [N II] λ 6584, and H α —which leaves a substantial fraction of emission-line galaxies unclassified due to quality requirements. As demonstrated by Cid Fernandes et al. (2010), many weak-line galaxies in large surveys such as the Sloan Digital Sky Survey (SDSS) lack reliable detections of all four diagnostic lines, particularly the weaker H β and [O III] features.

The WHAN diagram circumvents this limitation by utilizing only two lines, H α and [N II] λ 6584, which are generally the most prominent emission features in galaxy spectra. This economy enables classification of the large population of weak-line galaxies that would otherwise remain unclassified. Furthermore, the proximity of these two lines in wavelength space makes their ratio largely insensitive to dust extinction effects.

1.4.2 Physical Basis of the Classification Lines

The theoretical foundation of the WHAN diagram rests on the distinct ionization properties produced by different energy sources in galaxies. We now examine the physical reasoning behind each demarcation line.

The Star-Forming/AGN Boundary at $\log([\text{N II}]/\text{H}\alpha) = -0.4$ The vertical demarcation at $\log([\text{N II}]/\text{H}\alpha) = -0.4$ separates pure star-forming galaxies from systems with active galactic nuclei (AGN) or other non-stellar ionization sources. This boundary represents a transposition of the empirical SF/AGN dividing line established in BPT space by Stasińska et al. (2006).

The physical origin of this division lies in the fundamentally different spectral energy distributions (SEDs) of ionizing radiation from young massive stars versus AGN. In star-forming regions, photoionization is dominated by O and B stars with effective temperatures $T_{\text{eff}} \lesssim 50,000$ K. These stellar populations produce ionizing spectra that decline sharply beyond the Lyman limit, resulting in relatively low electron temperatures ($T_e \sim 10^4$ K) in the ionized gas (Kewley et al., 2001). Under these conditions, the secondary nitrogen enrichment characteristic of metal-rich galaxies produces [N II]/H α ratios that saturate at $\log([\text{N II}]/\text{H}\alpha) \approx -0.4$, even at supersolar metallicities (Kauffmann et al., 2003).

AGN, by contrast, generate power-law ionizing continua that extend to much higher photon energies. This harder radiation field produces a more extended partially ionized zone where collisionally excited forbidden lines such as [N II] are enhanced relative to recombination lines. The result is systematically higher [N II]/H α ratios, exceeding the theoretical maximum achievable by stellar photoionization alone (Kewley et al., 2006; Stasińska et al., 2006).

The Seyfert/LINER Division at $W_{\text{H}\alpha} = 6 \text{ \AA}$ The horizontal demarcation at $W_{\text{H}\alpha} = 6 \text{ \AA}$ separates Seyfert galaxies (strong AGN) from Low-Ionization Nuclear Emission-line Regions (LINERs). This boundary corresponds to a transposition of the Seyfert/LINER classification developed by Kewley et al. (2006) in the traditional BPT framework.

The physical interpretation of this division relates to the ionization power of the central source. Seyfert nuclei are luminous AGN with high ionizing photon fluxes that produce strong emission lines characterized by high equivalent widths. The $H\alpha$ equivalent width traces the ratio of ionizing photon flux to the underlying stellar continuum, with $W_{H\alpha} > 6 \text{ \AA}$ indicating a significant AGN contribution to the total ionizing budget.

LINERs, in contrast, exhibit weaker emission lines with $3 < W_{H\alpha} < 6 \text{ \AA}$. This class has historically been associated with low-luminosity AGN powered by radiatively inefficient accretion flows onto supermassive black holes (Ho, 2008). However, the WHAN diagram reveals that the LINER region encompasses two physically distinct populations that overlap in traditional BPT space: genuine weak AGN (wAGN) and so-called “retired galaxies” ionized by evolved stellar populations.

The Weak AGN/Retired Galaxy Boundary at $W_{H\alpha} = 3 \text{ \AA}$ A crucial innovation of the WHAN diagram is the identification of the $W_{H\alpha} = 3 \text{ \AA}$ boundary separating weak AGN from retired galaxies. This demarcation was established empirically through the observation of a bimodal distribution in $W_{H\alpha}$ among LINER-like systems (Cid Fernandes et al., 2011).

The theoretical basis for this division lies in the nature of ionizing radiation from hot low-mass evolved stars (HOLMES), including post-asymptotic giant branch (post-AGB) stars, planetary nebula nuclei, and extreme horizontal branch stars (Binette et al., 1994; Stasińska et al., 2008). These evolved stellar populations are ubiquitous in old stellar systems and produce a diffuse UV radiation field that can ionize ambient gas, generating weak emission lines with LINER-like ratios.

The critical insight of Stasińska et al. (2008) was that the integrated ionizing energy distribution from HOLMES is substantially harder than that of massive OB stars, resembling a $\sim 10^5 \text{ K}$ blackbody spectrum. This hard radiation field naturally produces the elevated $[NII]/H\alpha$ ratios characteristic of LINERs. However, the total ionizing luminosity from HOLMES is limited by the mass budget of evolved stars in old populations. As demonstrated by Cid Fernandes et al. (2011), the ratio of extinction-corrected $H\alpha$ luminosity to the $H\alpha$ luminosity expected from HOLMES photoionization (the parameter ξ) follows a strongly bimodal distribution: galaxies with $\xi \gg 1$ require additional ionization sources (star formation or AGN activity), while systems with $\xi \sim 1$ can be fully explained by HOLMES ionization alone.

The $W_{H\alpha} = 3 \text{ \AA}$ threshold marks the boundary below which HOLMES ionization suffices to explain the observed emission. Retired galaxies (RGs) are thus systems that have ceased forming stars but retain weak emission lines powered entirely by their old stellar populations. The term “retired” aptly describes galaxies that have retired from active star formation, distinguishing them from “passive” galaxies (see below) and from genuinely active systems hosting weak AGN (Stasińska et al., 2008).

Passive Galaxies Below $W_{H\alpha} = 0.5 \text{ \AA}$ The lowest equivalent width regime, $W_{H\alpha} < 0.5 \text{ \AA}$ and $W_{[NII]} < 0.5 \text{ \AA}$, defines truly passive (or “lineless”) galaxies. Below these thresholds, emission-line measurements become unreliable due to noise and continuum placement uncertainties. These systems represent the endpoint of galaxy evolution: massive ellipticals and S0 galaxies with purely old stellar populations and negligible warm gas reservoirs.

Interestingly, the similar physical properties of retired and passive galaxies—stellar mass, optical

colours, mean stellar age, and metallicity—suggest they share common evolutionary histories (Cid Fernandes et al., 2011). The primary difference appears to be gas content rather than stellar populations. As demonstrated by Herpich et al. (2018), both populations contain similar numbers of HOLMES producing comparable ionizing photon rates; the presence or absence of detectable emission depends on the availability of gas to be ionized. This gas may originate from accretion from circumgalactic reservoirs or residual streams from past merger events, explaining the observed differences between otherwise similar quiescent systems (Belfiore et al., 2016).

1.4.3 Practical Classification Criteria

Following the analysis of Cid Fernandes et al. (2011), the WHAN diagram identifies five classes of galaxies with distinct physical properties:

1. **Pure star-forming galaxies (SF):** $\log([\text{N II}]/\text{H}\alpha) < -0.4$ and $W_{\text{H}\alpha} > 3 \text{ \AA}$. These systems occupy the canonical H II region locus and are dominated by ionization from young massive stars.
2. **Strong AGN (Seyferts):** $\log([\text{N II}]/\text{H}\alpha) > -0.4$ and $W_{\text{H}\alpha} > 6 \text{ \AA}$. Galaxies hosting luminous active nuclei with significant contributions to the total ionizing radiation field.
3. **Weak AGN (wAGN):** $\log([\text{N II}]/\text{H}\alpha) > -0.4$ and $3 < W_{\text{H}\alpha} < 6 \text{ \AA}$. Systems with low-luminosity active nuclei, potentially powered by radiatively inefficient accretion.
4. **Retired galaxies (RG):** $W_{\text{H}\alpha} < 3 \text{ \AA}$ but $W_{\text{H}\alpha}$ or $W_{[\text{N II}]}$ $> 0.5 \text{ \AA}$. Former star-forming systems now ionized solely by HOLMES from their evolved stellar populations.
5. **Passive galaxies:** $W_{\text{H}\alpha} < 0.5 \text{ \AA}$ and $W_{[\text{N II}]} < 0.5 \text{ \AA}$. Truly quiescent systems lacking detectable emission lines.

1.4.4 Implications for Galaxy Evolution Studies

The WHAN classification scheme has profound implications for understanding galaxy evolution and the demographics of nuclear activity. By enabling robust separation of retired galaxies from genuine weak AGN, the diagram reveals that many objects previously classified as LINERs in BPT space are in fact “fake AGN”—systems whose emission arises from stellar rather than accretion processes (Cid Fernandes et al., 2011). This distinction is crucial for accurate census of AGN populations and for understanding the role of nuclear activity in galaxy quenching.

Furthermore, the continuity observed between strong AGN, weak AGN, and retired galaxies in the WHAN diagram suggests possible evolutionary connections. Comparative analyses of star formation histories across these classes corroborate the proposed differentiation and reveal similarities between strong and weak AGN on one hand, and between retired and passive galaxies on the other (Cid Fernandes et al., 2011). These patterns are consistent with scenarios where AGN activity accompanies the final stages of star formation quenching, followed by evolution into retired and ultimately passive states.

The WHAN diagram thus provides not only a practical classification tool but also a window into the physical processes governing the life cycles of galaxies and their central black holes.

2 The KMOS3D-Sample

The KMOS^{3D} survey is a 75-night guaranteed time program conducted with KMOS at the VLT (**Wisnioski2019**; Wisnioski et al., 2015). The survey targets the H α + [N II]+ [S II] emission lines in galaxies at $0.6 < z < 2.7$, providing spatially resolved measurements of ionized gas kinematics, star formation, and nebular conditions.

The complete KMOS^{3D} sample comprises 739 galaxies with $\log(M_*/M_\odot) > 9$ (**Wisnioski2019**). Targets were drawn from the mass-selected parent sample of the 3D-HST Treasury Survey (**Brammer2012**; **Skelton2014**), ensuring uniform coverage of the star formation–stellar mass (M_*) and rest-frame $(U - V)$ – M_* planes.

To resolve the internal dynamics of these distant systems, the KMOS3D survey was established as a five-year guaranteed time observation program using the K-band Multi-Object Spectrograph (KMOS) mounted on the Very Large Telescope (VLT) (**Sharples2013**). The survey targeted over 600 galaxies selected from the 3D-HST and CANDELS treasury programs, providing a mass-complete sample across the "Main Sequence" of star-forming galaxies (**Wisnioski2019**).

The KMOS3D survey is a comprehensive multi-year program designed to investigate the internal kinematics and physical properties of galaxies during the peak epoch of cosmic star formation ($z \approx 0.7 - 2.7$). Utilizing the K-band Multi-Object Spectrograph (KMOS) on the Very Large Telescope (VLT), the survey provides integral field spectroscopy (IFS) for over 600 galaxies (**Wisnioski2019**; Wisnioski et al., 2015).

2.1 Sample Selection and Redshift Ranges

Releases 2019 (Wisnioski et al., 2019) the KMOS3D is a subsample from the HST-observed galaxies, ensuring a mass-complete sample across the Main Sequence of galaxies, which can for example be seen in ?? The survey is divided into observations at four near-infrared bands, leading to observation of the H- α -line in three different redshift-regimes. The splitting in different redshifts is independent from the spacial splitting of our observations in three different fields, namely the COSMOS-, GOODS-S- and UDS-Field. Both splittings are shown in the Figure 4. We also observe a $\sim 10\%$ AGN-fraction according to the Million-Quasar-Catalog (**Flesch2015**). Another interesting fact about the analysis previously done at this sample is that previous teams (**todo**) were able to determine the redshift based on the KMOS3D-observations for $\sim 80\%$ of the galaxies. If possible we use the measured redshift from this data as a prior for our own determined redshift, otherwise we take the literature-taken values for this galaxies also given by **todo**

- $z \approx 0.9$: Observations at the Y- and J-band, corresponding accordingly to $\sim 1.02 - 1.12 \mu$ and $\sim 1.17 - 1.33 \mu\text{m}$ and leads to a look-back time of approximately 7.5 billion years.
- $z \approx 1.5$: Observations at the $\sim 1.49 - 1.78 \mu\text{m}$, corresponding to a look-back time of approximately 9.4 billion years.
- $z \approx 2.3$: K-Band $\sim 2.03 - 2.37 \mu\text{m}$ Corresponding to a look-back time of approximately 10.8 billion years, often referred to as "Cosmic Noon".

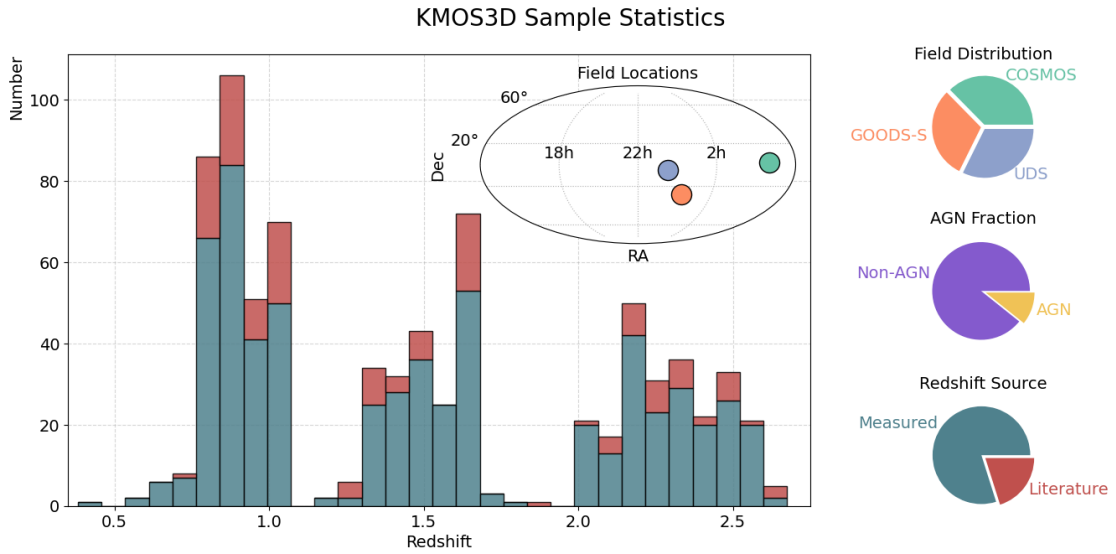


Figure 4: Statistical overview of the KMOS^{3D} galaxy sample. The main histogram shows the redshift distribution of the sample, which primarily covers the range $z \approx 0.6 - 2.7$. The stacked colors distinguish between redshifts measured by the KMOS^{3D} survey (teal) and those compiled from existing literature (red). The top-center inset displays the celestial coordinates of the three survey fields (GOODS-S, COSMOS, and UDS). The pie charts on the right provide a fractional breakdown of the sample, illustrating the distribution of galaxies across the three fields, the fraction of sources identified as hosting an Active Galactic Nucleus (AGN), and the overall proportion of measured versus literature-based redshifts.

3 The KMOS^{3D} Survey: Kinematics and Scaling Relations at Cosmic Noon

The KMOS^{3D} survey represents one of the most comprehensive efforts to date to characterize the internal kinematics and physical properties of star-forming galaxies (SFGs) during the peak of cosmic star formation ($z \sim 0.6-2.7$). By utilizing the K-band Multi-Object Spectrograph (KMOS) on the VLT, the survey provides spatially resolved $H\alpha$ emission maps for a mass-selected sample across the COSMOS, GOODS-S, and UDS fields (Wisnioski2019; Wisnioski et al., 2015).

3.1 Sample Properties and Scaling Relations

The survey target selection ensures a representative coverage of the galaxy population, spanning stellar masses of $\log(M_*/M_\odot) = 9.0-11.7$. As illustrated in Figure 5, the sample follows the established scaling relations of the "cosmic noon" epoch.

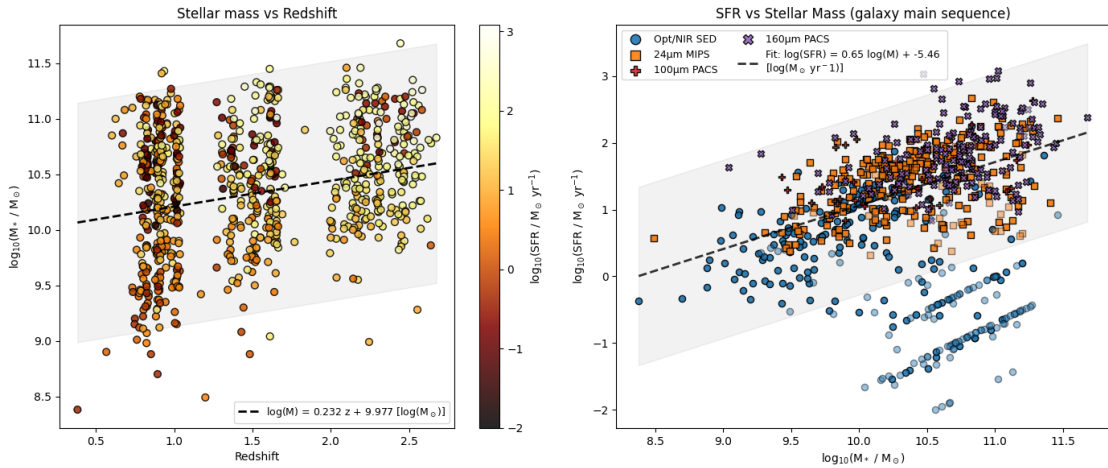


Figure 5: **Scaling relations for the KMOS^{3D} sample.** (Left) Stellar mass versus redshift, color-coded by star formation rate (SFR). A weak positive correlation reflects the survey’s selection function and the growth of galaxies over cosmic time. The dashed line denotes the best-fit linear relation with $\pm 2\sigma$ scatter (shaded). (Right) The star-forming main sequence (SFMS), demonstrating the tight correlation between SFR and M_* . Galaxies with KMOS^{3D} internal redshifts are shown in blue; literature redshifts in orange.

The star formation rates within the sample range from below $1 M_\odot \text{ yr}^{-1}$ to several hundred $M_\odot \text{ yr}^{-1}$. The distribution and redshift evolution of these SFRs, derived from a combination of Opt/NIR SED fitting and mid-to-far infrared photometry (MIPS $24\mu\text{m}$, PACS $100/160\mu\text{m}$), are shown in Figure 6.

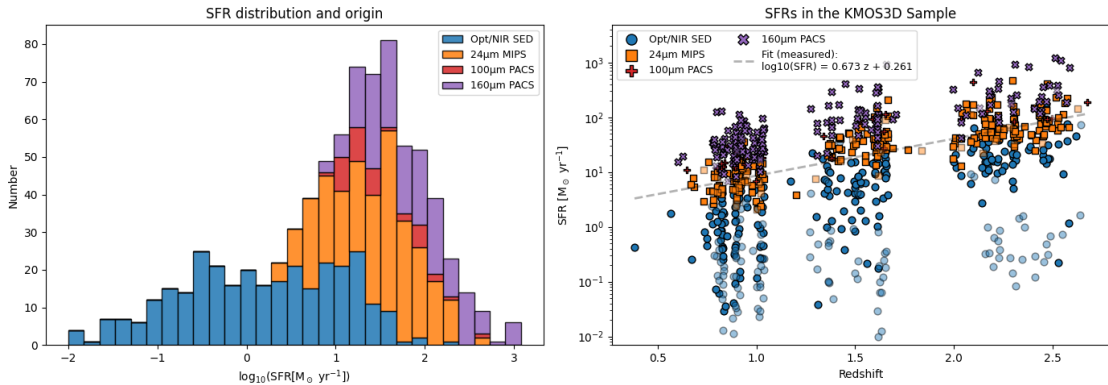


Figure 6: **SFR distribution and origin.** (Left) Histogram of SFRs across the sample, categorized by the primary observational indicator. The distribution peaks near $\sim 30 M_\odot \text{ yr}^{-1}$. (Right) Evolution of SFR with redshift, highlighting the systematic increase in star formation activity toward $z \sim 2.5$. The dashed line represents the best-fit relation $\log_{10}(\text{SFR}) = 0.673z + 0.261$.

3.2 Kinematic State and Disk Dominance

A fundamental finding of KMOS^{3D} is the high prevalence of ordered rotation. Using criteria based on monotonic velocity gradients and the ratio of rotation velocity to intrinsic dispersion (v_{rot}/σ_0), Wisnioski2019<empty citation> found that approximately 77% of the full sample is rotation-dominated.

This high fraction of disk-like systems suggests that the star-forming main sequence is primarily composed of rotating gas disks rather than chaotic major mergers. However, these high- z disks differ significantly from local spirals:

- **Elevated Turbulence:** Intrinsic velocity dispersions evolve as $\sigma_0 \propto (1+z)$, decreasing from $\sim 50 \text{ km s}^{-1}$ at $z \sim 2.3$ to $\sim 25 \text{ km s}^{-1}$ at $z \sim 0.9$. This is consistent with marginally stable disk theory (Toomre1964; Genzel2011).
- **Geometric Thickness:** Low v_{rot}/σ_0 ratios (typically 2–5, compared to 10–20 in the local universe) imply geometrically thick, pressure-supported configurations.
- **Baryon Dominance:** Massive SFGs at this epoch are often baryon-dominated within the effective radius, leading to declining outer rotation curves as dark matter plays a secondary dynamical role (Lang2017; Genzel2020).

3.3 Internal Dynamics: Inflows and Outflows

Beyond global rotation, KMOS^{3D} reveals the complex baryonic cycle within galaxies. Forward modeling of the "RC100" sub-sample has identified radial streaming motions ($v_r \sim 30\text{--}90 \text{ km s}^{-1}$), providing direct evidence for the "violent disk instability" scenario where gas is driven inward to form central bulges (Dekel2009; Genzel2023).

Simultaneously, the survey provides a census of galactic outflows. Förster Schreiber et al. (2019) identified high-velocity components in approximately one-third of the sample:

- **SF-driven winds:** Ubiquitous across mass scales with $\eta \sim 0.1\text{--}0.2$.
- **AGN-driven winds:** Predominantly found in massive systems ($\log(M_*/M_\odot) > 10.7$), reaching velocities of 1000 - 2000 km s^{-1} .

The detection of broad-line components beneath the $\text{H}\alpha$ profile allows for the spatial resolution of these feedback processes, offering a "high-resolution laboratory" to study the quenching mechanisms that ultimately shape the Hubble sequence. The full KMOS 3D Survey (KMOS^{3D}) dataset, encompassing 739 galaxies, remains a foundational resource for understanding galaxy assembly at cosmic noon.

4 Analysis

4.1 PSF-Cleaning

We began our analysis by PSF-cleaning the data cubes to compensate for the influence of beam smearing on our results. This was achieved by multiplying each slice of the cube by the given PSF from (Wisnioski et al., 2019). The PSF was aligned and rebinned to the spaxel grid of the cube itself prior to multiplication, as illustrated in Figure 7.

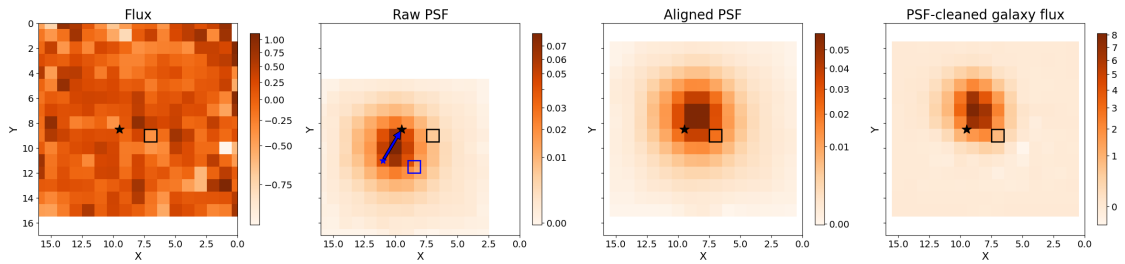


Figure 7: Representation of the PSF-cleaning process via Multiplication with the given PSF from Wisnioski et al., 2019. The calculation was done after the necessary alignment and therefore rebinning of the PSF with the cube’s spaxel-grid.

We tested an artificial enlargement of the pixel scale by not rebinning the PSF pixel, but discarded it due to the low SNR of the single spaxel, and because the PSF is only given for spatial dimensions, and important features such as the shape of the emission line are not changed, but redistributed to four smaller pixels. We also shifted the data to the rest frame using the redshift estimated by spectroscopy in KMOS^{3D}Data Release and the following formula:

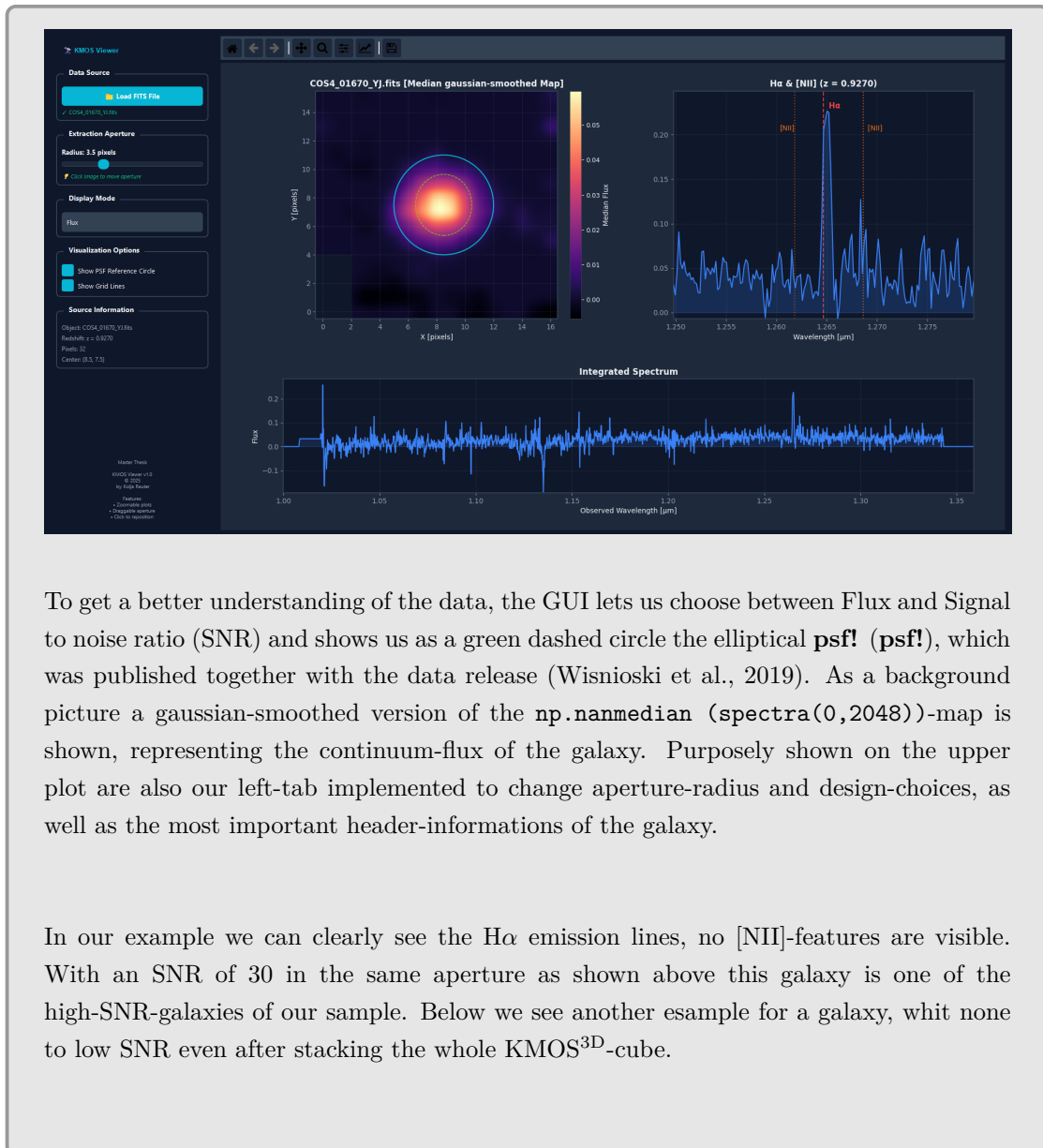
$$\lambda_{rest} = \lambda_{obs}/(1 + z). \quad (7)$$

. If no spectroscopic redshift was available, we used the literature value published in the data release. The fraction of these redshifts is close to 20%, which is particularly evident in Figure 4. The literature sources come from the 3D-HST catalogue at the time of target selection. (van Dokkum et al., 2013; Wisnioski et al., 2019)

From now on, when we refer to the data, we are always referring to the PSF-cleaned data. When we refer to wavelengths or present spectra, we are always referring to rest-frame wavelengths in μm , i.e. we have already corrected for the redshift of the respective galaxy, unless otherwise noted. To further investigate the PSF-cleaned data, we created a small GUI to quickly stack spectra within a radius and position that can be chosen freely. This allows us to quickly assess the data quality and the general spectral features of our sample. An example output of this GUI can be seen below.

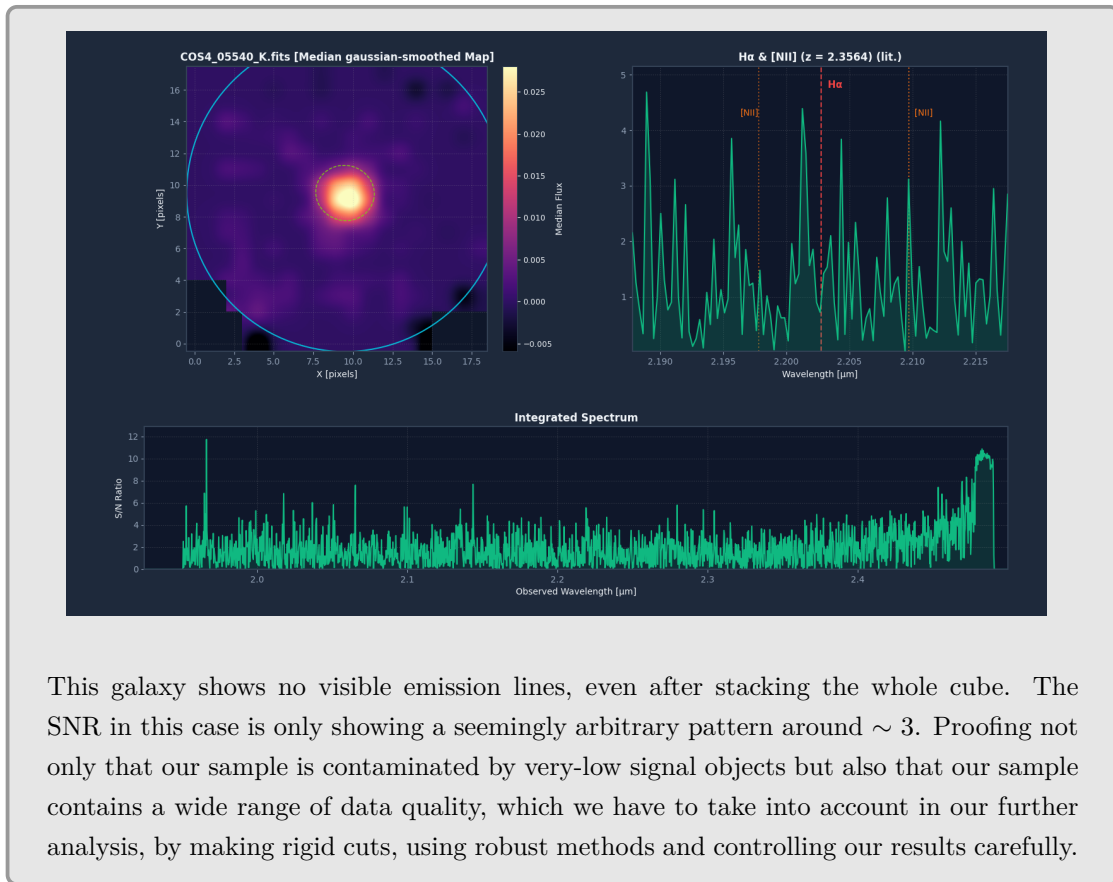
GUI 1 - Investigating stacked spectra

To get a first overview of the data quality and the general spectral features of our sample, we created a small graphical user interface (GUI) that allows us to quickly stack the spectra of all spaxels within a free-choosable radius around a free-choosable position. This allows us to get a quick overview of the data quality and the general spectral features of our sample. An example output of this GUI can be seen in in the following.



To get a better understanding of the data, the GUI lets us choose between Flux and Signal to noise ratio (SNR) and shows us as a green dashed circle the elliptical **psf!** (**psf!**), which was published together with the data release (Wisnioski et al., 2019). As a background picture a gaussian-smoothed version of the `np.nanmedian(spectra(0,2048))`-map is shown, representing the continuum-flux of the galaxy. Purposely shown on the upper plot are also our left-tab implemented to change aperture-radius and design-choices, as well as the most important header-informations of the galaxy.

In our example we can clearly see the H α emission lines, no [NII]-features are visible. With an SNR of 30 in the same aperture as shown above this galaxy is one of the high-SNR-galaxies of our sample. Below we see another example for a galaxy, with none to low SNR even after stacking the whole KMOS^{3D}-cube.



4.2 Voronoi binning

To ensure the reliability of the derived spectroscopic parameters, particularly in the faint outskirts of the observed galaxies where the SNR in individual pixels may fall below the threshold required for stable non-linear least-squares minimization, we employ a Voronoi 2D binning technique. By spatially co-adding spectra within Voronoi cells, we reached **roughly** the target SNR of 5, allowing for a robust decomposition of the emission line profiles.

Although the underlying IFU data is represented by a rigid grid of square pixels, the Voronoi tessellation-algorithm (Cappellari & Copin, 2003) uses an adaptive network of polygons to better reflect the local signal-to-noise distribution. Each polygon is mathematically defined by the perpendicular bisectors between adjacent bin centroids, ensuring that any point within a given cell is closer to its own generator than to any other generator. This polygonal representation effectively smooths the jagged boundaries of individual pixel clusters, providing a continuous visual summary of the galaxy's physical structure that is free from grid-level noise distractions. Allowing the geometry to adapt to the data density means that the Voronoi bins clearly illustrate the transition from high-resolution central regions to lower-resolution outskirts, where larger area integration is required. Consequently, using polygons emphasises the adaptive nature of the binning algorithm and highlights the spatial scales over which spectral information has been co-added to reach the target sensitivity. The presence of bins with a signal-to-noise ratio (S/N) below the requested target is primarily a consequence of the initial S/N threshold used to define the 'good' pixel mask. During the binning process, if an individual pixel's S/N is al-

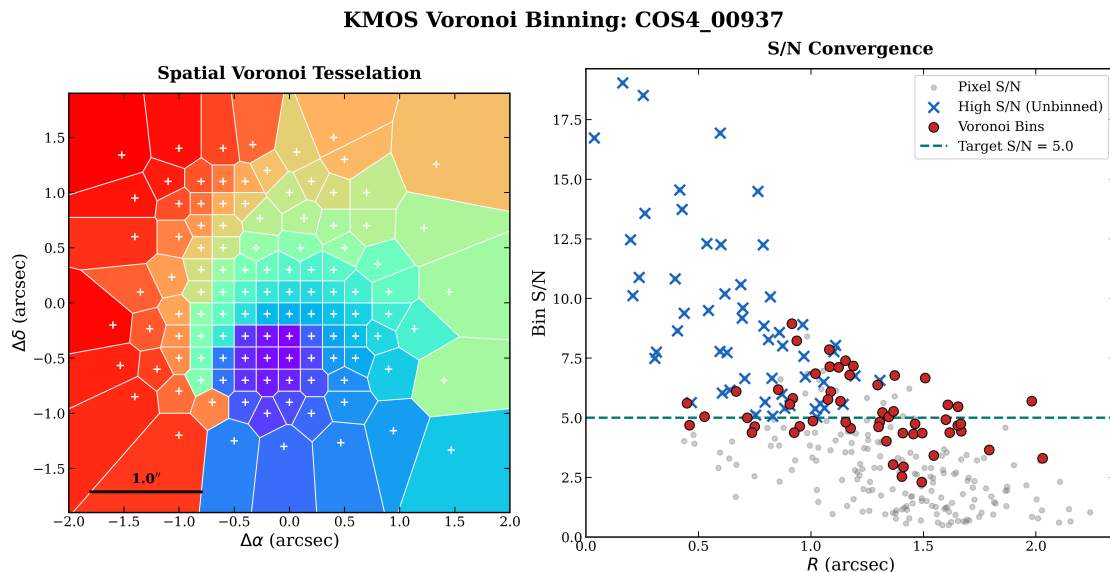


Figure 8: Adaptive Voronoi binning of COSMOS 00937 emission line data calibrated to a target S/N of 5.0. On the left, the spatial map displays the adaptive tessellation, where bin area scales inversely with local flux to maintain uniform sensitivity across the field; white crosses indicate bin centroids and the scale bar represents $1.0''$. On the right, the radial distribution shows the co-addition of low- S/N pixels (gray) into optimized Voronoi bins (red) to meet the target threshold (dashed teal line). Blue crosses identify high- S/N pixels that met the criteria independently, while bins remaining below the threshold represent the physical limit of the data at the mask boundaries where insufficient signal exists for further co-addition.

ready very low, it may be assigned to a bin that cannot mathematically reach the target after co-adding several neighbours without incorporating pixels that are too distant. Furthermore, the algorithm prioritises the ‘compactness’ of bins and will stop adding pixels to a bin if doing so would create an elongated or non-contiguous shape, even if the target S/N hasn’t been met. In the outermost regions of the galaxy, where flux drops exponentially, there are often insufficient valid pixels remaining to aggregate into a bin that satisfies the S/N requirement. Consequently, these ‘undershot’ bins represent the physical limit of the data. A more in-depth description can be found in Cappellari and Copin, 2003.

4.3 Emission line fitting

Our first crucial step of analysis was to fit the $H\alpha$ and $[NII]$ emission lines. Due to the data quality, we employed a multi-Gaussian ansatz with up to two Gaussians per emission line. The methodology, implemented in a specialized numerical framework, is designed to extract precise kinematic and flux information from Integral Field Spectroscopy (IFS) data. The following description outlines the physical and mathematical rationale behind the algorithmic steps.

4.3.1 Continuum Estimation

Before fitting the emission lines, the local continuum is modeled using a linear approximation:

$$f_{\text{cont}}(\lambda) = a\lambda + b \quad (8)$$

The algorithm utilizes a resilient background estimation by masking the H α and [NII] emission complex (0.6535–0.6600 μm) and calculating the continuum from the remaining spectral windows. A sigma-clipping procedure (3σ rejection based on the median absolute deviation) is applied to remove outliers before performing a linear fit. This ensures that the underlying stellar population continuum and residual instrumental signatures are accounted for without overestimating the emission line flux.

4.3.2 Emission Line Models

The core analysis fits the H α ($\lambda 6562.8 \text{ \AA}$) and the [NII] doublet ($\lambda\lambda 6548, 6583 \text{ \AA}$) using an adaptive hierarchical fitting strategy.

Table 1: Boundaries for model parameters

Parameter/Constant	Value/Constraint	Physical Reason
H α	0.656281 μm	Atomic transition reference
[NII] $\lambda 6583$	0.6583 μm	Doublet red component
[NII] $\lambda 6548$	0.6548 μm	Doublet blue component
[NII] Flux Ratio	2.96 : 1 (fixed)	Quantum transition probabilities
H α Center Range	0.6550–0.6575 μm	Must lie between [NII] lines
Narrow σ	0.8–4.0 \times pixel size	Resolve turbulent disk motions
Broad σ	2.5–6.0 \times pixel size	Outflows/non-circular motions
Amplitude Constraint	> 0 (absolute)	Physical emission flux

Single-Component Model (Triple Gaussian) In the first instance, a triple-Gaussian model is applied where the kinematics of H α and [NII] are coupled:

$$f(\lambda) = G_{\text{H}\alpha}(\lambda; A_{\text{H}\alpha}, \sigma, \lambda_0) + G_{6583}(\lambda; A_{\text{NII}}, \sigma, \lambda_0 + \Delta\lambda_{6583}) + G_{6548}(\lambda; A_{\text{NII}}/R, \sigma, \lambda_0 + \Delta\lambda_{6548}) \quad (9)$$

where $G(\lambda; A, \sigma, \mu) = A \exp[-(\lambda - \mu)^2 / (2\sigma^2)]$ denotes a Gaussian profile, $\Delta\lambda_{6583} = \lambda_{[\text{NII}]6583} - \lambda_{\text{H}\alpha}$ and $\Delta\lambda_{6548} = \lambda_{[\text{NII}]6548} - \lambda_{\text{H}\alpha}$ are the fixed wavelength offsets, and $R = 2.96$ is the theoretical [NII] doublet ratio.

- **Coupled Velocity:** H α and [NII] lines are assumed to originate from the same ionized gas clouds, thus sharing the same line-of-sight velocity (centroid shift λ_0) and velocity dispersion (σ). This coupling reduces the number of free parameters (from 9 to 4), making the model more suitable for the typical signal-to-noise ratio in our data. This approach is commonly employed when fitting the H α + [NII] complex, e.g. Lopes, A. R. et al., 2025.
- **Doublet Ratio:** The flux ratio of the [NII] lines is not fixed to the theoretical value of 2.96 ($f_{6583}/f_{6548} \approx 3$), dictated by the ratio of the transition probabilities from the same excited state, but set as a free parameter ranging from 2.7 up to 3.3, following the suggestions from Dojčinović et al., 2023, where it is described that in galaxie observation of high Signal-to-noise data a value of 3.1 is much more likely to observe, also due to overlap with the H α line wing. An overlap that is also in our data pretty common.
- **Center Constraint:** The H α centroid is constrained to lie between the two [NII] rest wavelengths ($0.6550 < \lambda_0 < 0.6575 \mu\text{m}$), ensuring physically meaningful solutions.

The fitting procedure employs multiple initial parameter guesses spanning different values of σ (1.2–3.0 pixel widths) and [NII]/H α amplitude ratios (0.15–0.45), selecting the solution with the lowest χ^2 .

Double-Component Model For regions with more complex dynamics, a second, broader Gaussian component is introduced for H α :

$$f(\lambda) = G_{\text{H}\alpha,\text{n}}(\lambda; A_1, \sigma_1, \lambda_1) + G_{6583} + G_{6548} + G_{\text{H}\alpha,\text{b}}(\lambda; A_2, \sigma_2, \lambda_2) \quad (10)$$

where subscripts “n” and “b” denote the narrow and broad components, respectively. The [NII] doublet remains kinematically coupled to the narrow H α component.

The narrow component represents the undisturbed (mainly corcular rotating) part of the gaseous disk, while the broader component ($\sigma_{\text{broad}} > 1.3 \times \sigma_{\text{narrow}}$) is physically attributed to non-circular motions, such as galactic-scale outflows, stellar feedback processes or high turbulence in central regions. Both H α centroids are independently constrained to lie within the physical bounds (0.6550–0.6575 μm).

The fitting algorithm performs a Monte-Carlo-Simulation over narrow widths (1.2–2.4 pixel sizes), broad widths (3.0–5.0 pixel sizes), and amplitude fractions, applying strict post-fit validation:

1. Both centroids must remain within the allowed wavelength range
2. The broad component must satisfy $\sigma_{\text{broad}} > 1.3 \times \sigma_{\text{narrow}}$
3. The combined model must reproduce at least 50% of the observed peak amplitude
4. Total H α amplitude must exceed 40% of the peak

4.3.3 Fit Quality Assessment

The fitting is performed using the Levenberg-Marquardt algorithm, for some people better known as (damped) least-squares-method. To ensure physical solutions, amplitudes are constrained to be positive and centroids are restricted to prevent the algorithm from fitting noise spikes or OH-sky line residuals. For every fit, we calculate the reduced chi-squared (χ_{red}^2):

$$\chi_{\text{red}}^2 = \frac{1}{\nu} \sum \frac{(f_{\text{obs}} - f_{\text{model}})^2}{\sigma_{\text{noise}}^2} \quad (11)$$

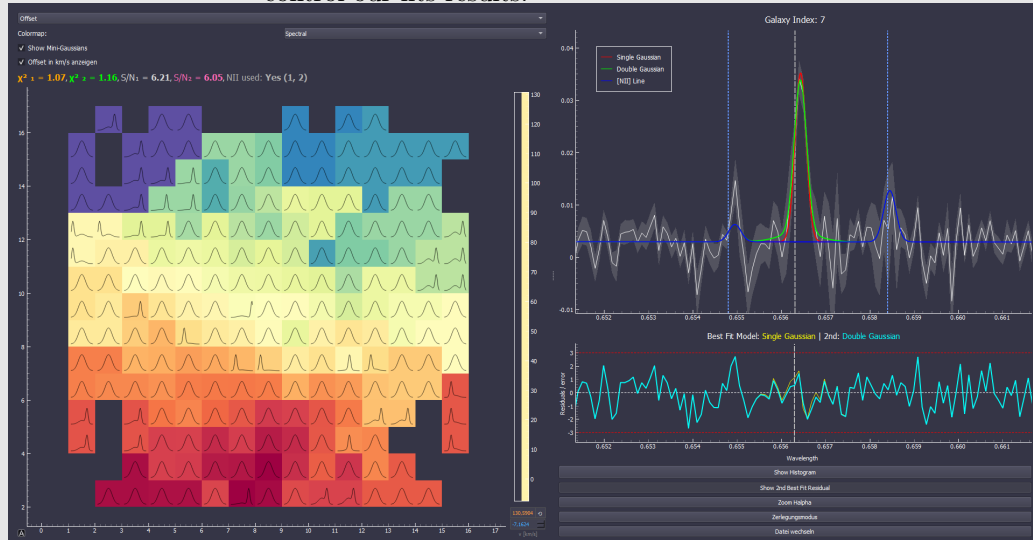
where ν represents the degrees of freedom. This metric allows for automated model selection, ensuring that a double-gaussian component is only accepted if it significantly improves the fit quality over a single-component model.

4.3.4 Adaptive Fitting Strategy

The analysis employs an adaptive approach: the combined H α + [NII] fit is attempted first. If this yields a valid result with $\chi_{\nu}^2 < 50$, it is accepted. Otherwise, the algorithm falls back to a single H α -only Gaussian fit. For each bin, both single- and double-component fits are performed, with the results stored separately for subsequent analysis of kinematic complexity.

GUI 2 - Presenting the fitting results via PyQT

The second GUI that we built was an fast-acting visualisation program to show and control our fits-results.



In this Graphical User Interface (GUI) we can see on the left side the spaxel-map of COSMOS Galaxy 02167, observed in the YJ-band of K-band Multi-Object Spectrograph (KMOS). We look at the colorcoded velocity and see two major points:

- The galaxy shows a clear velocity-gradient from the upper right to the lower left corner, indicating a rotating disk. rotating slowly with ~ 60 km/s around the central velocity.
- The central velocity calculated by the given redshift from KMOS^{3D} seems to be 60 km/s (or 1.5 \AA) off, although the redshift was flagged as secured estimated reshift from the same data.

On the right side we see the spectrum of the currently selected spaxel, overplotted with our fit-results, as well as residuals and second-best fit-residuals. The most important fit-quality information is shown above the map. We also can quickly name the most important implemented features of this GUI:

- Free choose of a variety of cmap's from the `Matplotlib.colormaps`-repertoire, as well as `vmin` and `vmax` adjustments.
- Switching between different fitted parameters, e.g. $H\alpha$ -Flux, Velocity Dispersion, Velocity, Fitting-Quality-indicators such as SNR and χ_{red}^2 for different components, as well as single- and double-component fits.
- Fast file switching by indexing through the whole sample.
- Adding second-best fit residuals to the residual-spectra as well as decomposing multi-gaussians into their single components for better visualisation of e.g. the broad-line component.

- Displaying a histogram of the residuals, overplotted with a red normal distribution to quickly evaluate and eliminate systematic fitting errors.
- Showing and hiding small black gaussians to quickly find areas of disturbed emission lines and therefore areas of high interest.
- Switching between km/s and $\Delta\lambda$ for velocity-dispersion and velocity-maps.



Even in this seemingly undisturbed galaxy we can see some spaxels with a clear broad-line component, as shown in the example spectrum above. With a W80-value in this spaxel of 428 km/s this spaxel is already in the regime of possible AGN-activity or strong outflow. Although it is clearly visible for us that even when the fitting algorithm is, due to the high-noise in the regime as well as some data points that are lying below the continuum-fit, maybe underestimating the strength of the [NII]-doublet. This shows us that we have to be very careful when we interpret our results, as well as that we have to control our fitting-results very carefully, especially in the low-SNR regime, which is unluckily the regime where we expect to find most of the interesting physical processes in the search for fossil outflows.

4.4 W80-Analysis and Galaxy Classification

We used the in [described W80-parameter](#) to build a sub-sample of galaxies with higher chance of having a second component of H α gas. Later we will further discuss whether this component is induced by AGN-activity or other physical processes. Due to the fact that we need to induce different catalogs to completely exclude the chance of falsely-negative AGNs we used PyQT 5 to build a GUI to visually classify the galaxies. Figure 9 shows a screenshot of the GUI, where we can see on the left side the W80-distribution of our sample, overplotted means, as well as gaussian distributions and a colorcoding following the Million-Quasar-Catalog by Flesch, 2023.

add paragraph here

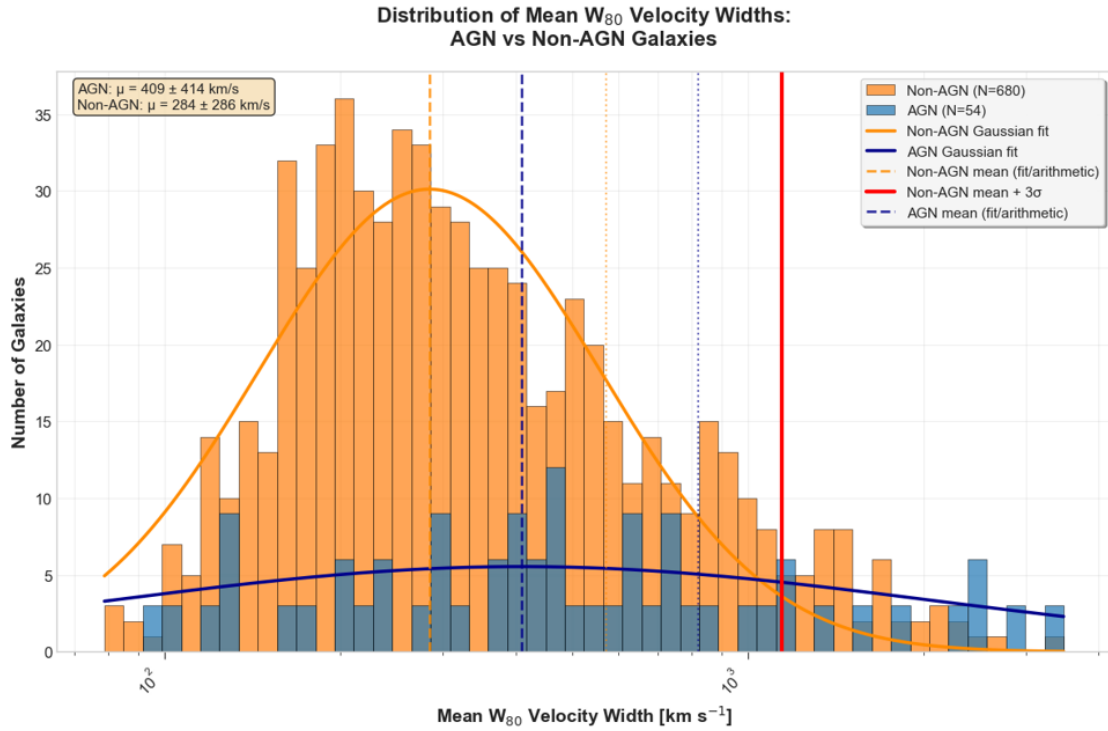


Figure 9: tbd

GUI 3 - W80 Distribution and Classification

The third GUI built is an improved version of the `Matplotlib widget` or `Matplotlib qt` environment, specialising in displaying distributions. In our case we use it to display W80-distributions, colorcoded by the Simbad-Classification or the Classification according to the Million Quasar catalogue. The building of an GUI for this purpose allows us to show discrete distributions with nearly the same calculation time, independent of size, as well as continuous distributions. The first is most clearly visible when we look at our implemented function for splitting the distribution, which changes from showing galaxy means to showing every spaxel. Here, one must bear in mind the linguistic imprecision that one spaxel in the GUI corresponds to one Voronoi bin and therefore comprises a minimum of one spaxel in the data cube. This results in calculation time changes from 0.8 to 1.3 seconds for binary classifications (like showing every galaxy within or without the Million Quasar catalogue) for all 586 galaxies or when we show Simbad it changes from 7.9 to 10 seconds when we change the loading time from Galaxies ($N = 586$) to displaying every spaxel ($N = 8089$). Due to the fact that our sample does not intrinsically have a distribution of galaxy types, we have implemented a way to show trends in galaxy types, by convolving the discrete distribution with a normal-distribution where σ is calculated based on the standard deviation of the discrete sample.

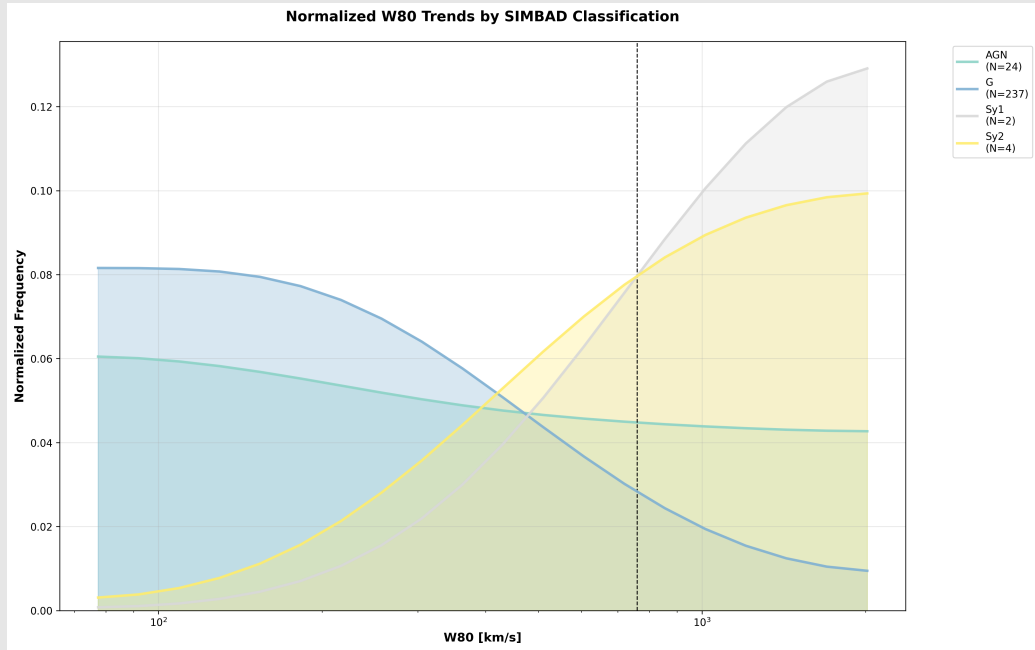
$$f(x) = (P * G)(x) \quad (12)$$

where:

$$P(x) = \sum_{i=1}^n w_i \delta(x - x_i) \quad (13)$$

$$G(x, \sigma) = \frac{1}{\sigma\sqrt{2\pi}} \exp\left(-\frac{x^2}{2\sigma^2}\right) \quad (14)$$

$$\sigma = \sigma_{distr} = \sqrt{\sum_{i=1}^n w_i (x_i - \mu)^2} \quad (15)$$



Scoping the range of this thesis this tool allows us this way to look at known trends of

W80-parameters against galaxy types, allowing us in the future also to be more sure when we classify galaxies based on their W80-parameters. We can easily see for example how Seyfert 1 galaxies have the highest W80-values on average, followed by Seyfert 2 galaxies and AGN. While regular galaxies have the lowest W80-values on average. Even

better is seen that in our sample the W80-values of AGN is ranging about the whole spectrum from regular galaxies to Seyfert 1 galaxies, showing that in an AGN higher W80-values dont need to be dominant, but can be found as well as lower W80-values.

This is an important fact to keep in mind when we later want to discuss the search for fossil outflows.

Table 2: W80 statistics according to simbad classes

SIMBAD class	N Galaxies	N Spaxel	Mean (km/s)	Median (km/s)
AG?	8	74	397.8	319.6
AGN	16	331	257.0	166.4
BiC	2	61	223.6	210.5
CIG	1	2	175.6	175.6
EmG	100	2506	243.3	188.7
G	237	4467	230.8	167.5
Q?	1	16	289.4	210.4
QSO	2	101	316.4	262.3
SN*	1	9	292.0	231.8
Sy1	2	28	1454.5	1551.6
Sy2	4	55	854.3	835.3
rG	16	428	283.8	200.5

add description of the pybabbarolo-fitting here

5 Results

5.1 Statistical Overview of the Sample

Our emission-line fitting analysis encompasses 586 galaxies spanning a redshift range of $0.6 < z < 2.57$, with a median redshift of $z = 1.30$. The total number of Voronoi bins analysed amounts to 32,564, providing spatially resolved spectroscopic information across the sample. In this section, we present a comprehensive statistical characterization of the fitting results, including assessments of fit quality, signal-to-noise distributions, and the derived emission-line properties.

5.1.1 Fit Quality Assessment

The quality of our Gaussian emission-line fits is evaluated through the reduced chi-squared statistic (χ_ν^2), which provides a measure of goodness-of-fit normalized by the degrees of freedom. For an ideal fit with correctly estimated uncertainties, χ_ν^2 should be distributed around unity.

Figure 10 presents the per-bin χ_ν^2 distributions for both single and double Gaussian fits. The single Gaussian fits (left panel) show a distribution peaking near $\chi_\nu^2 \approx 1.2$ with a tail extending toward higher values, based on 31,862 bins. The double Gaussian fits (right panel), applied to 13,480 bins where a second kinematic component was warranted, display a similar distribution centred slightly above unity. Both distributions indicate that our fitting procedure produces statistically acceptable results for the majority of spatial bins, with the slight positive offset potentially attributable to residual systematic effects or underestimated uncertainties in certain spectral regions.

At the galaxy level, Figure 11 summarizes the χ_ν^2 statistics aggregated per galaxy. The left and right panels show the distributions of mean χ_ν^2 values for single and double Gaussian fits, respectively. While a few galaxies exhibit elevated mean χ_ν^2 values—indicative of systematically poor fits, potentially due to complex emission-line profiles, low signal-to-noise, or contamination—the majority cluster near low values. The central panel displays the distribution of the best (minimum) χ_ν^2 achieved per galaxy, which peaks around $\chi_\nu^2 \approx 0.8$, demonstrating that for each

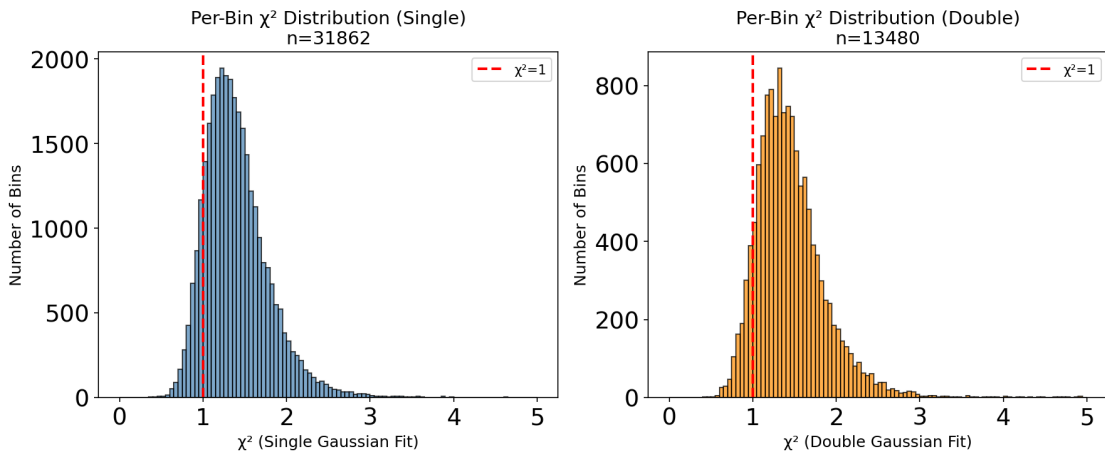


Figure 10: Per-bin reduced chi-squared (χ_ν^2) distributions for single Gaussian fits (left, blue; $n = 31,862$ bins) and double Gaussian fits (right, orange; $n = 13,480$ bins). The red dashed line marks $\chi_\nu^2 = 1$, corresponding to an ideal fit. Both distributions peak near unity, indicating overall good fit quality across the sample.

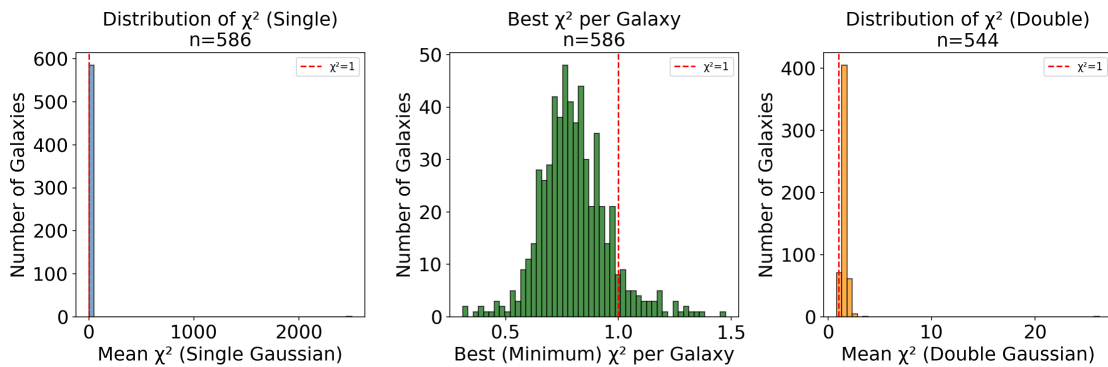


Figure 11: Galaxy-level χ_ν^2 statistics. *Left*: Distribution of mean χ_ν^2 from single Gaussian fits across 586 galaxies. *Centre*: Distribution of the best (minimum) χ_ν^2 achieved per galaxy, peaking below unity. *Right*: Distribution of mean χ_ν^2 from double Gaussian fits for 544 galaxies where such fits were performed.

galaxy at least some spatial bins yield excellent fits.

The relationship between fit quality and signal-to-noise ratio (S/N) is explored in Figure 12. For both single and double Gaussian fits, we observe that χ_ν^2 values cluster around unity across a wide range of S/N, with increased scatter at low S/N ($S/N < 1$). At higher S/N, the χ_ν^2 distribution tightens, as expected when the data more strongly constrain the model. The absence of a strong systematic trend between χ_ν^2 and S/N indicates that our fitting procedure performs robustly across the dynamic range of our data.

5.1.2 Signal-to-Noise Characteristics

The signal-to-noise ratio of the H α emission line is a critical parameter governing the reliability of derived quantities. Figure 13 presents the S/N distributions for both fitting approaches. The single Gaussian S/N distribution (left panel) is heavily weighted toward low values, with the majority of bins having $S/N < 3$. The double Gaussian fits (right panel), which are preferentially

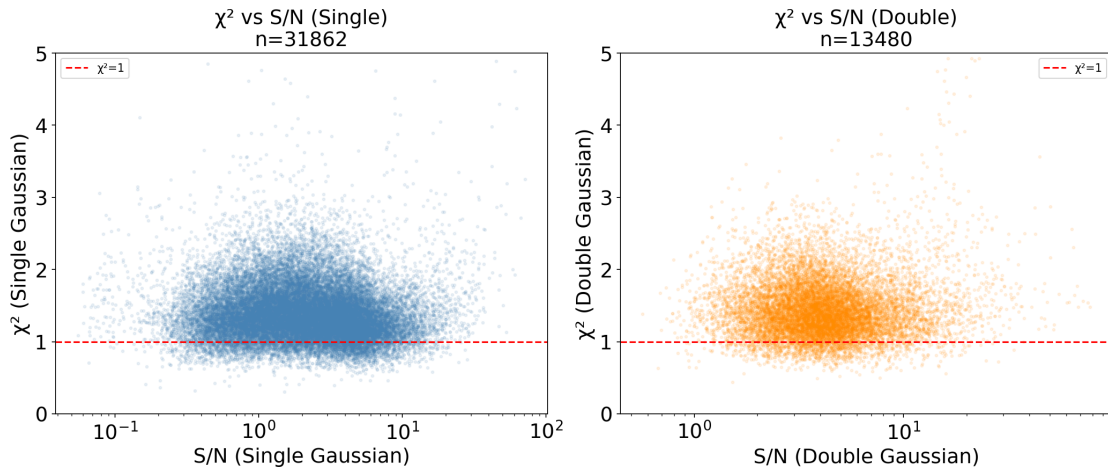


Figure 12: Reduced chi-squared versus signal-to-noise ratio for single Gaussian fits (left, blue) and double Gaussian fits (right, orange). The red dashed line indicates $\chi^2_\nu = 1$. No strong systematic dependence is observed, indicating robust fitting performance across the S/N range.

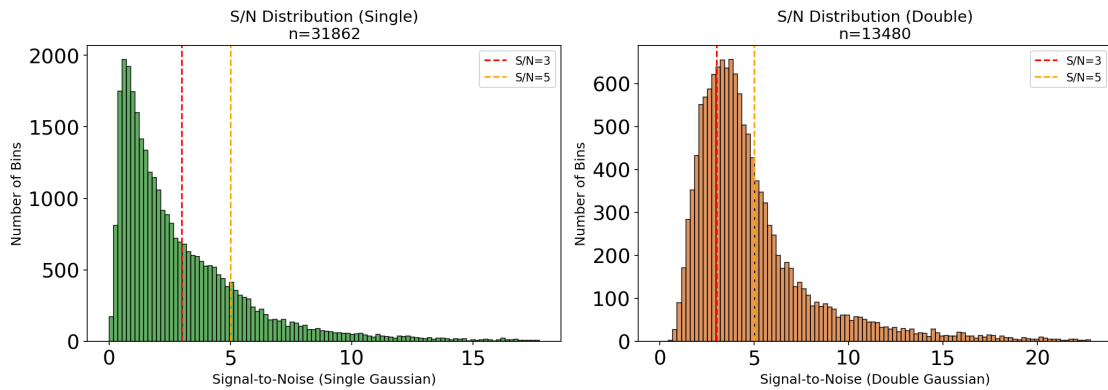


Figure 13: Signal-to-noise ratio distributions of the H α emission line for single Gaussian fits (left, green; $n = 31,862$) and double Gaussian fits (right, orange; $n = 13,480$). Vertical dashed lines indicate commonly adopted detection thresholds at S/N = 3 (red) and S/N = 5 (yellow).

applied to bins with stronger emission, show a distribution shifted toward higher S/N values, peaking around S/N ≈ 3 –5.

5.1.3 Emission-Line Properties

The distribution of H α amplitudes provides insight into the range of emission-line strengths across our sample. Figure 14 shows these distributions at both galaxy-averaged (left) and per-bin (right) levels. The galaxy-level distribution spans approximately two orders of magnitude, from $\log_{10}(\text{Amplitude}) \approx -3.8$ to -1.8 , with a peak around -2.8 . The per-bin distribution extends to lower amplitudes, reflecting the inclusion of outer galaxy regions with fainter emission.

5.1.4 Kinematic Properties

The velocity dispersion of the ionized gas, derived from the Gaussian line widths after accounting for instrumental broadening, provides information on the dynamical state of the emitting regions.

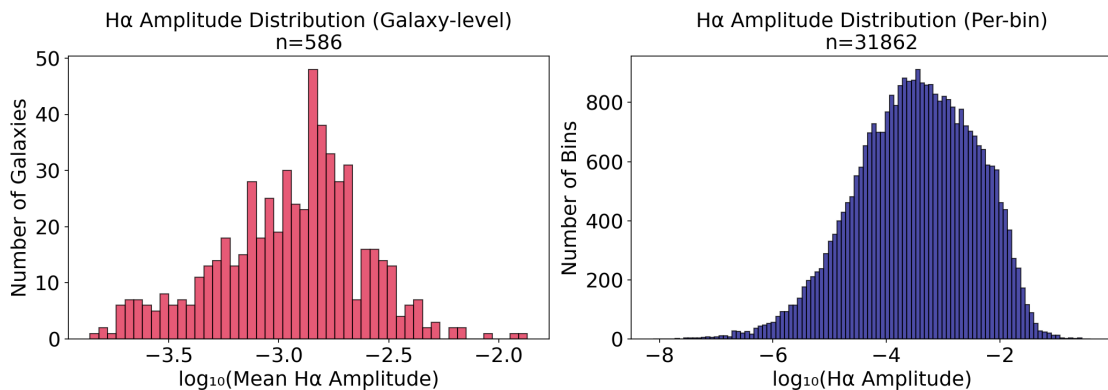


Figure 14: Distribution of H α amplitudes at the galaxy level (left, pink; $n = 586$ galaxies showing mean amplitudes) and per spatial bin (right, blue; $n = 31,862$ bins). The broader range at the per-bin level reflects the radial decline of emission-line surface brightness.

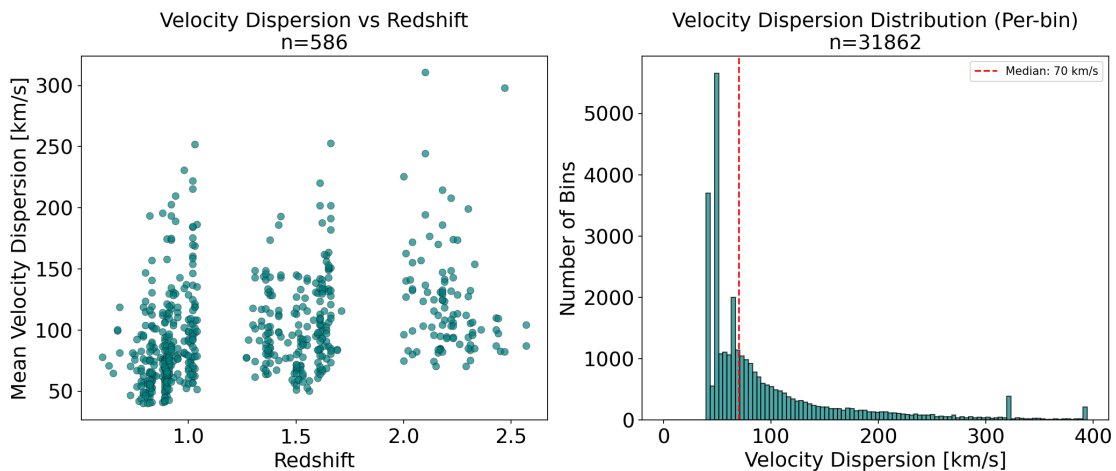


Figure 15: *Left*: Mean velocity dispersion per galaxy as a function of redshift for the 586 galaxies in our sample. *Right*: Per-bin velocity dispersion distribution ($n = 31,862$), with a median of 70 km s^{-1} indicated by the red dashed line.

Figure 15 presents the velocity dispersion as a function of redshift (left panel) and its overall distribution (right panel). We find a median velocity dispersion of $\sigma = 70 \text{ km s}^{-1}$ at the per-bin level, with values typically ranging from 40 to 150 km s^{-1} . No strong evolution with redshift is apparent within our sample, though the discrete redshift distribution reflects the spectroscopic survey targeting strategy.

For galaxies where double Gaussian fits were applied, we additionally compute the non-parametric line width W_{80} , defined as the velocity width containing 80% of the total line flux. This metric is particularly sensitive to the presence of broad wings indicative of outflows or other non-gravitational motions. Figure 16 shows the relationship between H α flux and W_{80} (left panel), colour-coded by redshift, along with the W_{80} distribution (right panel). The median W_{80} of 205 km s^{-1} is consistent with moderately broadened lines, while the tail extending to $W_{80} > 500 \text{ km s}^{-1}$ suggests the presence of outflow signatures in a subset of galaxies, predominantly at higher redshifts and H α luminosities.

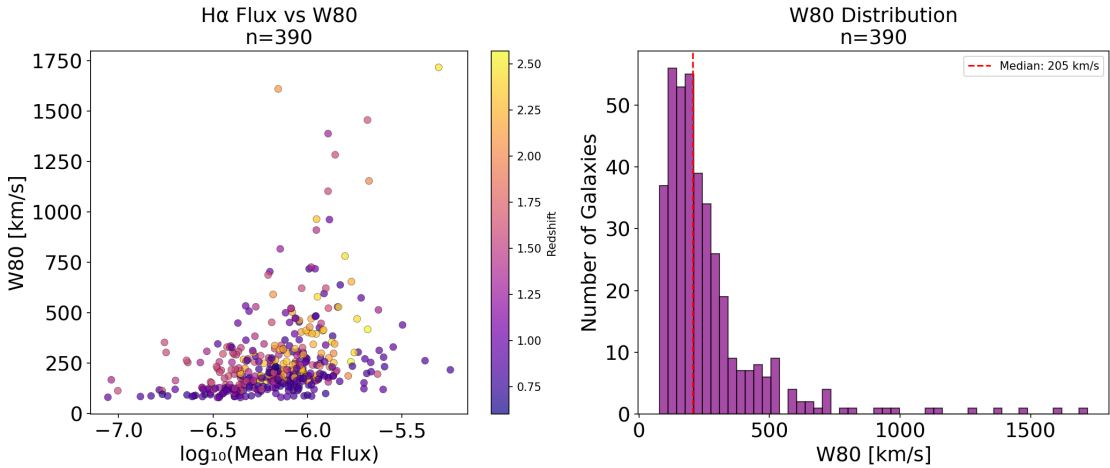


Figure 16: *Left*: Non-parametric line width W_{80} versus mean H α flux for 390 galaxies with double Gaussian fits, colour-coded by redshift. Higher W_{80} values at elevated fluxes and redshifts may indicate outflow activity. *Right*: Distribution of W_{80} , with a median of 205 km s⁻¹ (red dashed line).

5.1.5 The [N II]/H α Ratio and AGN Diagnostics

A key diagnostic ratio accessible from our spectral fitting is [N II] λ 6583/H α , which serves as a proxy for the hardness of the ionizing radiation field and gas-phase metallicity. In the classical BPT diagram (Baldwin et al., 1981), this ratio is combined with [O III] λ 5007/H β to distinguish star-forming galaxies from AGN. However, as [O III] and H β fall outside our observed spectral range for much of the sample, we cannot construct a full BPT classification. Instead, we examine the [N II]/H α ratio in combination with other available diagnostics.

Figure 17 presents the [N II]/H α ratio as a function of H α flux at both galaxy-averaged and per-bin levels. The vertical dashed lines indicate characteristic [N II]/H α thresholds derived from the BPT demarcation lines. Specifically, adopting the Kewley et al. (2001) maximum starburst line and solving for the [N II]/H α intercept at $\log_{10}([\text{O III}]/\text{H}\beta) = -0.1$ yields $\log_{10}([\text{N II}]/\text{H}\alpha) \approx 0.0$. Similarly, the Kauffmann et al. (2003) empirical line gives $\log_{10}([\text{N II}]/\text{H}\alpha) \approx -0.4$ under the same assumptions. While these thresholds are only approximate in the absence of the full BPT information, they provide useful reference points: galaxies with $\log_{10}([\text{N II}]/\text{H}\alpha) > 0$ are likely AGN-dominated, while those with $\log_{10}([\text{N II}]/\text{H}\alpha) < -0.4$ are consistent with pure star formation.

5.1.6 WHAN Diagram Classification

To provide a more complete classification of the ionization mechanisms in our sample, we employ the WHAN diagram (Cid Fernandes et al., 2011), which combines the H α equivalent width with the [N II]/H α ratio (see Section ?? for a detailed discussion of the theoretical background). This diagnostic has the advantage of requiring only two emission lines and is particularly well-suited to our dataset.

Figure 18 presents the WHAN diagram for our sample at both galaxy-averaged (left) and per-bin (right) levels. The standard demarcation lines separate the diagram into regions corresponding to star-forming galaxies (upper left), Seyfert AGN (upper right), LINER/weak AGN (lower right),

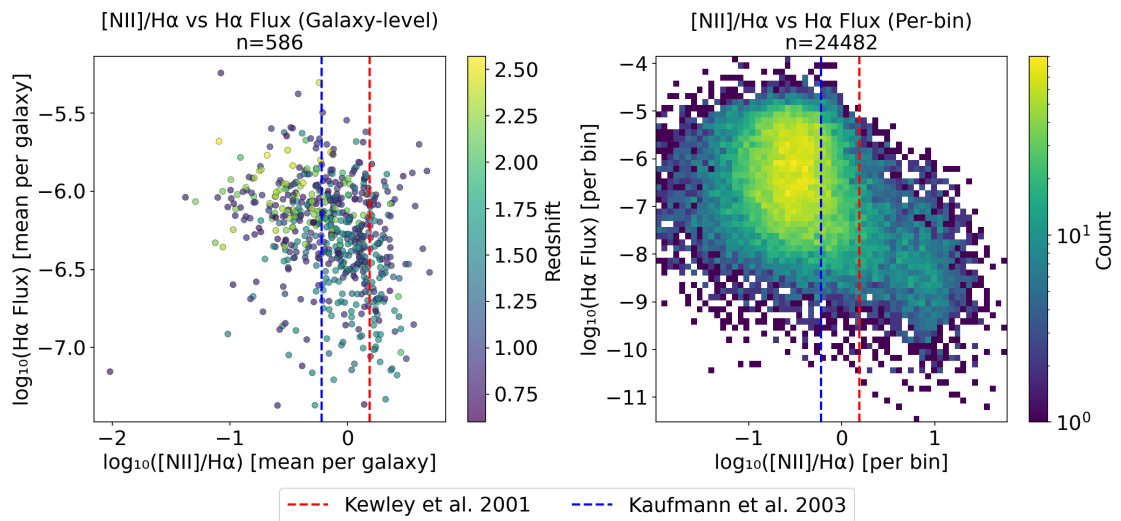


Figure 17: $[\text{NII}]/\text{H}\alpha$ ratio versus $\text{H}\alpha$ flux at the galaxy level (left; $n = 586$, colour-coded by redshift) and per spatial bin (right; $n = 24,482$, shown as a 2D histogram). Vertical dashed lines indicate approximate thresholds derived from the Kewley et al. (2001) (red) and Kauffmann et al. (2003) (blue) BPT demarcation lines (see text).

and retired/passive galaxies (bottom). At the galaxy level, we find a substantial population in the star-forming region, with a significant fraction also occupying the Seyfert and LINER domains. The per-bin analysis reveals the full complexity of spatially resolved ionization conditions, with individual galaxies often spanning multiple classification regions—consistent with the presence of central AGN activity surrounded by star-forming discs, or radial gradients in ionization conditions.

5.1.7 Summary Statistics

Table 3 summarizes the key statistical properties of our emission-line fitting results. The sample comprises 586 galaxies with a median redshift of $z = 1.30$ and spans 32,564 Voronoi bins. The median reduced chi-squared values of $\chi^2_\nu \approx 1.3$ – 1.4 for both single and double Gaussian fits indicate overall good fit quality. The kinematic analysis yields a median W_{80} of 205 km s^{-1} , while the median $[\text{NII}]/\text{H}\alpha$ ratio of 0.24 (corresponding to $\log_{10}([\text{NII}]/\text{H}\alpha) \approx -0.6$) places the typical galaxy in our sample in the star-forming regime of the BPT diagram.

⚠ Disclaimer about the usability of the data

necessary??

5.2 The search for fossil outflows in non-AGN galaxies

5.3 The Search for Fossil Outflows in Non-AGN Galaxies

A central goal of this work is to identify signatures of past AGN-driven outflows in galaxies that do not currently exhibit AGN activity—so-called “fossil outflows”. These relics of previous episodes of nuclear activity may manifest as broadened emission-line profiles, asymmetric line

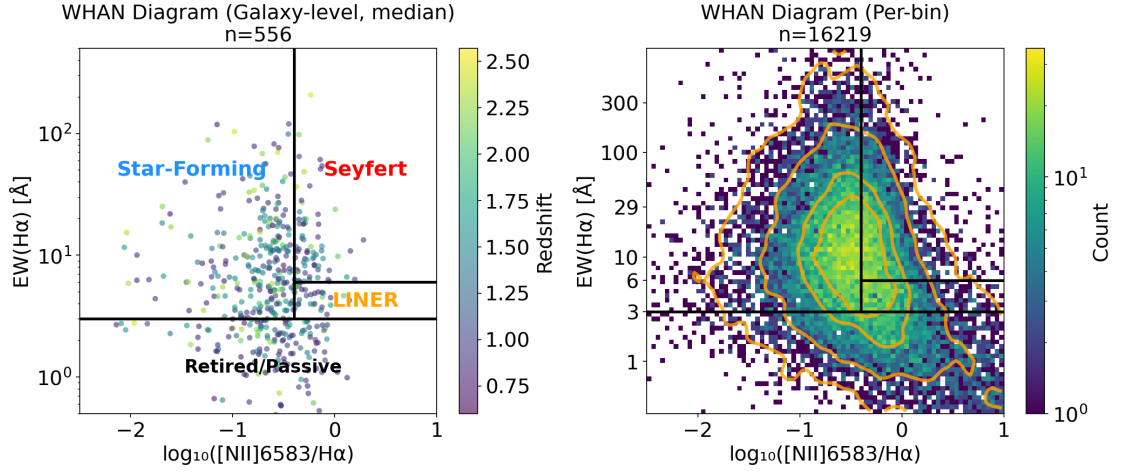


Figure 18: WHAN diagnostic diagram showing $H\alpha$ equivalent width versus $[NII]\lambda 6583/H\alpha$ ratio. *Left*: Galaxy-level median values ($n = 556$), colour-coded by redshift. *Right*: Per-bin measurements ($n = 16,219$) shown as a 2D histogram with density contours. The demarcation lines separate star-forming, Seyfert, LINER, and retired/passive galaxy regions following Cid Fernandes et al. (2011).

Table 3: Summary statistics of the Gaussian emission-line fitting results.

Parameter	Mean	Median	σ	Range
Total Galaxies		586		
Total Voronoi Bins		32,564		
χ^2_ν (Single Gaussian)	3.78	1.34	253.8	—
χ^2_ν (Double Gaussian)	1.49	1.39	2.20	—
W_{80} [km s ⁻¹]	266.5	205.1	213.8	—
$[NII]/H\alpha$	0.88	0.24	2.57	—

wings, or spatially extended regions of elevated velocity dispersion that persist after the central engine has faded. In this section, we present a selection of candidate galaxies from our sample that display kinematic signatures consistent with fossil outflow activity despite lacking current AGN classifications in standard catalogues.

Our candidate selection is based on a combination of criteria: (i) elevated W_{80} values indicative of non-Gaussian line profiles, (ii) detection of secondary broad $H\alpha$ components in the double Gaussian fits, (iii) spatial coherence of the kinematic anomalies suggesting organised outflow structures rather than noise, and (iv) absence of AGN signatures in the Milliquas catalogue and SIMBAD database, though we note that WHAN classifications may indicate Seyfert-like ionization in some cases, potentially reflecting residual AGN activity or HOLMES ionization of outflowing gas.

We now present detailed descriptions of eight candidat

5.4 The Search for Fossil Outflows in Non-AGN Galaxies

A central goal of this work is to identify signatures of past AGN-driven outflows in galaxies that do not currently exhibit AGN activity—so-called “fossil outflows”. These relics of previous episodes of nuclear activity may persist long after the central engine has faded, as AGN-driven outflows possess significant inertia and can continue expanding for $\sim 10^5$ – 10^6 yr after the AGN switches off (A. R. King et al., 2011; Zubovas, 2018; Zubovas & Maskeliunas, 2023). Indeed, semi-analytical estimates suggest that fossil outflows may comprise up to 60% of all observed galactic outflows (Zubovas et al., 2022).

In this section, we present a selection of candidate galaxies from our sample that display kinematic signatures consistent with fossil outflow activity despite lacking current AGN classifications. All candidates presented here are negative in both the Milliquas quasar catalogue and the SIMBAD astronomical database, indicating no evidence for current AGN activity from multi-wavelength observations.

5.4.1 Observational Criteria for Fossil Outflows

Following the theoretical framework of Zubovas and Maskeliunas (2023), who performed hydrodynamical simulations of AGN outflow evolution after the central engine switches off, we identify fossil outflow candidates based on the following observational signatures:

1. **Lopsided morphology:** Fossil outflows tend to become asymmetric as they propagate through an inhomogeneous interstellar medium, with the two outflow lobes often located at different position angles relative to the nucleus rather than forming a symmetric bipolar structure.
2. **Spatial detachment from the nucleus:** Unlike actively-driven outflows that remain connected to the central engine, fossil outflows can become spatially detached as they coast outward after the AGN fades. This manifests as broadened emission or elevated W_{80} values at positions offset from the galactic centre.
3. **Absence of current AGN signatures:** By definition, fossil outflows occur in galaxies where the AGN has switched off. We therefore require that candidates show no AGN

signatures in the Milliquas catalogue (which compiles quasars and AGN from multiple surveys) or SIMBAD.

4. **Elevated line widths:** The presence of a secondary broad $H\alpha$ component or elevated W_{80} values ($\gtrsim 300 \text{ km s}^{-1}$) indicates non-gravitational gas motions consistent with outflowing material.
5. **Spatial coherence:** The kinematic anomalies should show spatial coherence across multiple bins, indicating organised structure rather than noise fluctuations.

Importantly, Zubovas and Maskeliunas (2023) predict that fossil outflows should be more common in gas-poor galaxies and may outnumber actively-driven outflows by a factor of several in the local Universe, with potentially higher fractions at high redshift. Our sample, spanning $0.6 < z < 2.6$, is therefore well-suited to search for these elusive structures.

We now present detailed descriptions of eight candidate galaxies, ordered by the strength and clarity of their fossil outflow signatures.

5.4.2 U4_13108_H: A Compelling Fossil Outflow Candidate

Our most promising candidate is the galaxy U4_13108_H at $z = 1.31$ (Figure 19). This object displays remarkably clear spectroscopic signatures of broad, non-Gaussian $H\alpha$ emission across the central regions of the galaxy. The emission-line profile in the nuclear region shows pronounced asymmetry, with extended wings that cannot be adequately described by a single Gaussian component. The double Gaussian fit yields $\chi_1^2 = 1.52$ and $\chi_2^2 = 1.00$, demonstrating significant improvement when a second broad component is included.

The spatially resolved analysis reveals that the broadened emission is not confined to a single spaxel but extends coherently across multiple spatial bins, predominantly on the western side of the galaxy. This lopsided distribution of the broad component is consistent with the theoretical predictions of Zubovas and Maskeliunas (2023) for fossil outflows propagating through an inhomogeneous medium. The W_{80} map shows values reaching $\sim 1000 \text{ km s}^{-1}$ in the regions of strongest line broadening, while the velocity field exhibits a gradient consistent with an organised kinematic structure. The mean W_{80} of 259 km s^{-1} across the galaxy places it among the most kinematically disturbed objects in our sample.

Cross-matching with external catalogues confirms that this galaxy shows no evidence of current AGN activity: it is not identified in the Milliquas database and is classified simply as ‘‘Galaxy’’ in SIMBAD. The WHAN diagram classification suggests Seyfert-like ionization ratios in some regions, which may indicate shock-ionization of gas in the outflow itself rather than ongoing nuclear activity—a phenomenon also predicted by the simulations.

5.4.3 GS4_20422_K: Spatially Extended Broad $H\alpha$ Emission

The galaxy GS4_20422_K at $z = 2.00$ presents compelling evidence for a secondary, very broad $H\alpha$ component that appears to be kinematically decoupled from the [N II] emission (Figure 20). This decoupling is particularly significant, as it suggests that the broad emission originates from a distinct physical region—potentially an outflow that has become detached from the narrow-line region, as predicted by the fossil outflow models.

Figure 19: Emission-line analysis of the fossil outflow candidate U4_13108_H at $z = 1.31$. *Upper panels:* Spatially resolved maps of H α flux (left), W_{80} line width (centre), and line-of-sight velocity (right). The green cross marks the selected spaxel shown in the spectrum below. *Lower panel:* Extracted spectrum around the H α + [N II] complex showing the data (white), single Gaussian fit (red), and double Gaussian fit (green). The broad, asymmetric H α profile and the significant improvement of the double Gaussian fit ($\chi_2^2 = 1.00$ vs. $\chi_1^2 = 1.52$) provide strong evidence for a secondary kinematic component. This galaxy is negative in both SIMBAD and Milliquas, indicating no current AGN activity.

Figure 20: Same as Figure 19, but for GS4_20422_K at $z = 2.00$. This galaxy shows a very broad secondary H α component that appears decoupled from the [N II] emission, detected at multiple positions across the galaxy—consistent with the spatial detachment predicted for fossil outflows. The third map displays the [N II] flux distribution. The galaxy is negative in both SIMBAD and Milliquas.

The double Gaussian decomposition reveals a broad H α component with $\chi_1^2 = 1.64$ and $\chi_2^2 = 1.61$ at multiple positions throughout the galaxy, indicating that the secondary component is detected across spatially extended regions rather than being confined to the nucleus. This spatial detachment from the centre is a key signature of fossil outflows according to Zubovas and Maskeliunas (2023). The W_{80} map shows elevated values exceeding 1000 km s^{-1} in the central and northern regions, with a coherent spatial distribution suggestive of bipolar outflow morphology.

The flux map reveals a centrally concentrated H α distribution, while the [N II] flux map (right panel) shows a more extended and asymmetric morphology. This spatial offset between H α and [N II] emission further supports the interpretation that the broad H α component traces outflowing material with different ionization conditions than the ambient interstellar medium. The galaxy is negative in both SIMBAD and Milliquas.

5.4.4 U4_34515_YJ: Red-winged Asymmetry and Widespread Secondary Components

U4_34515_YJ at $z = 1.02$ exhibits a distinctive red-winged asymmetry in its H α profile, contrasting with the more commonly observed blue-shifted outflow signatures (Figure 21). The spectrum shows clear evidence for a secondary H α component shifted to longer wavelengths relative to the systemic velocity, potentially indicating receding outflow material on the far side of the galaxy.

The double Gaussian fitting procedure yields detections of a secondary component across a large fraction of the spatial bins, with $\chi_1^2 = 1.38$ and $\chi_2^2 = 1.21$ for the displayed spaxel. The widespread detection of secondary components throughout the galaxy is consistent with a fossil outflow that has had time to propagate across extended regions after the AGN switched off. The W_{80} map reveals moderately elevated values throughout the galaxy, with the highest values ($\sim 800 \text{ km s}^{-1}$) concentrated in the central regions. The velocity map shows a clear gradient across the galaxy, consistent with ordered rotation, upon which the broader component is superimposed.

The prevalence of secondary component detections across this galaxy makes it a particularly valuable object for studying the spatial extent and geometry of the putative fossil outflow structure. The galaxy is negative in both SIMBAD and Milliquas.

Figure 21: Same as Figure 19, but for U4_34515_YJ at $z = 1.02$. This galaxy displays a red-winged $H\alpha$ asymmetry and numerous detections of a secondary component across the spatial extent of the galaxy, consistent with an evolved fossil outflow. The galaxy is negative in both SIMBAD and Milliquas.

Figure 22: Same as Figure 19, but for COS4_06327_YJ at $z = 0.80$. A flat but clearly detected broad component is measured between $H\alpha$ and the high-wavelength [N II] line, extending across nearly the entire eastern side of the galaxy in a lopsided distribution characteristic of fossil outflows. The galaxy is negative in both SIMBAD and Milliquas.

5.4.5 COS4_06327_YJ: Broad Component Between $H\alpha$ and [N II]

The galaxy COS4_06327_YJ at $z = 0.80$ shows a distinctive broad emission component situated between the $H\alpha$ and [N II] $\lambda 6583$ lines (Figure 22). While relatively flat in profile, this component is clearly detected above the noise level and extends across nearly the entire eastern half of the galaxy—a lopsided distribution characteristic of fossil outflows.

The spectral fitting reveals $\chi_1^2 = 2.03$ and $\chi_2^2 = 1.82$, with the double Gaussian model providing a notably better description of the data in the inter-line region. The spatial distribution of this broad component, concentrated on one side of the galaxy, is consistent with the asymmetric morphologies predicted by Zubovas and Maskeliunas (2023) for outflows that have decoupled from their driving source and propagate preferentially through lower-density channels in the ISM.

The [N II] flux map shows enhanced emission coincident with the regions of elevated W_{80} , suggesting that the outflowing gas may be shock-heated, consistent with the prediction that fossil outflows should show enhanced cooling and potentially different ionization properties than actively-driven counterparts. The galaxy is negative in both SIMBAD and Milliquas.

5.4.6 U4_29207_YJ: Bipolar Blue and Red Wings

U4_29207_YJ at $z = 0.83$ presents intriguing evidence for spatially separated blue-shifted and red-shifted broad components, potentially indicating a bipolar outflow structure (Figure 23). The southwestern region of the galaxy shows signatures of a blue-winged $H\alpha$ component, while a much weaker red-winged component is detected in the northeastern quadrant. This lopsided bipolar morphology, with asymmetric lobes at different position angles, matches the theoretical predictions for fossil outflows.

The double Gaussian fit yields $\chi_1^2 = 1.19$ and $\chi_2^2 = 1.18$, with relatively modest improvement over the single Gaussian model reflecting the subtlety of the broad component in this object. However, the spatial anti-correlation between blue-shifted and red-shifted excess emission provides compelling evidence for an organised kinematic structure rather than random noise fluctuations. The W_{80} map shows the characteristic pattern with regions of elevated line widths surrounding the nucleus but not centred on it—potentially indicating detachment from the central engine as predicted for fossil outflows. The velocity map reveals a clear rotational signature, with the outflow components oriented roughly perpendicular to the major kinematic axis of the galaxy. The galaxy is negative in both SIMBAD and Milliquas.

Figure 23: Same as Figure 19, but for U4_29207_YJ at $z = 0.83$. This galaxy shows evidence for a blue-winged $H\alpha$ component in the southwestern region and a weaker red-winged component in the northeast, forming a lopsided bipolar structure consistent with fossil outflow predictions. The galaxy is negative in both SIMBAD and Milliquas.

Figure 24: Same as Figure 19, but for COS4_17395_YJ at $z = 1.09$. A predominantly blue-winged component is detected above the noise level from the central-right region extending toward the upper-centre of the galaxy, showing spatial coherence consistent with fossil outflow structure. The galaxy is negative in both SIMBAD and Milliquas.

5.4.7 COS4_17395_YJ: Persistent Blue Wing Detection

COS4_17395_YJ at $z = 1.09$ exhibits predominantly blue-shifted excess emission in its $H\alpha$ profile, detected across multiple spatial bins from the central-right region extending toward the upper-centre of the galaxy (Figure 24). While the broad component is relatively flat, it consistently hovers above the noise level in the affected regions.

The fitting statistics ($\chi_1^2 = 1.37$ and $\chi_2^2 = 1.17$) indicate meaningful improvement when the second component is included. The spatial coherence of the blue-wing detections, forming a connected region rather than scattered isolated pixels, strengthens the case for a physical origin. The elongated, asymmetric distribution of the broad component is consistent with a fossil outflow that has preferentially expanded along a low-density channel in the ISM.

The velocity field shows complex structure that may reflect the superposition of rotation and outflow kinematics. The W_{80} values are moderately elevated ($\sim 600\text{--}800 \text{ km s}^{-1}$) in the regions of blue-wing detection, consistent with the presence of high-velocity gas. The galaxy is negative in both SIMBAD and Milliquas.

5.4.8 U4_15499_YJ: Horizontal Kinematic Structure with Enhanced [N II]

U4_15499_YJ at $z = 0.92$ displays subtle but spatially coherent signatures of a blue-winged $H\alpha$ component oriented along the horizontal axis of the galaxy, with intriguingly enhanced [N II] emission in the orthogonal direction (Figure 25). This geometric arrangement may indicate a relationship between outflow direction and the distribution of shock-ionized or metal-enriched gas.

The mean W_{80} of 305 km s^{-1} places this object among the more kinematically disturbed galaxies in our sample. The double Gaussian fit ($\chi_1^2 = 1.76$, $\chi_2^2 = 1.39$) shows substantial improvement over the single-component model.

The perpendicular arrangement of the kinematic disturbance (horizontal) and [N II] enhancement (vertical) could arise from several physical scenarios consistent with fossil outflows, including gas that has been shock-heated along the outflow propagation axis, or a more complex three-dimensional geometry where the outflow has become detached and lopsided as it expanded through the ISM. The galaxy is negative in both SIMBAD and Milliquas.

Figure 25: Same as Figure 19, but for U4_15499_YJ at $z = 0.92$. Weak signatures of a blue-winged $H\alpha$ component are detected along the horizontal axis, while enhanced [N II] emission is observed in the orthogonal direction. The galaxy is negative in both SIMBAD and Milliquas.

Figure 26: Same as Figure 19, but for COS4_15698_YJ at $z = 1.09$. A horizontal band of elevated W_{80} values passes through the galactic nucleus, potentially representing a younger fossil outflow that has not yet fully detached from the central region. The galaxy is negative in both SIMBAD and Milliquas.

5.4.9 COS4_15698_YJ: Nuclear Outflow with Possible Coupling

The final candidate in our selection, COS4_15698_YJ at $z = 1.09$, shows a horizontal band of elevated W_{80} values passing through the galactic nucleus (Figure 26). Unlike some of the other candidates where the broad component appears spatially detached from the centre, this structure remains connected to the nuclear region, suggesting this may represent a younger fossil outflow that has not yet fully decoupled from its origin.

The spectral analysis yields $\chi_1^2 = 1.37$ and $\chi_2^2 = 1.17$, with the double Gaussian fit capturing excess flux in the wings of the $H\alpha$ profile. The linear morphology of the elevated W_{80} region, extending across the nucleus rather than being centrally concentrated, suggests a collimated outflow or jet-like structure.

According to the framework of Zubovas and Maskeliunas (2023), this object may represent an intermediate evolutionary stage where the AGN has recently switched off but the outflow has not yet had sufficient time to fully detach and develop the characteristic lopsided morphology of older fossil outflows. The galaxy is negative in both SIMBAD and Milliquas.

5.4.10 Summary of Fossil Outflow Candidates

Table 4 summarizes the properties of our eight fossil outflow candidates. The sample spans a redshift range of $0.80 < z < 2.00$ and exhibits a variety of kinematic signatures including blue-shifted wings, red-shifted wings, bipolar structures, and spatially extended broad components. Critically, all candidates are negative in both the Milliquas AGN catalogue and SIMBAD, confirming the absence of current AGN activity and supporting the fossil outflow interpretation.

The observed properties of our candidates—lopsided morphologies, spatial detachment or offset from the nucleus, and elevated line widths—are consistent with the theoretical predictions of Zubovas and Maskeliunas (2023) for the evolution of AGN-driven outflows after the central engine switches off. Given that their simulations predict fossil outflows should outnumber actively-driven ones by a factor of several, and that our high-redshift sample may have even higher fossil fractions, the identification of eight candidates in our sample of 586 galaxies represents a detection rate of $\sim 1.4\%$, broadly consistent with expectations given detection limitations.

These candidates represent the most promising targets for follow-up observations aimed at confirming the fossil outflow interpretation. Higher spectral resolution observations would enable more precise decomposition of the line profiles, while integral field spectroscopy with broader wavelength coverage could provide access to additional diagnostic lines such as [O III] and $H\beta$ for full BPT classification. Deep imaging observations might also reveal morphological signatures of past interaction or merger events that could have triggered the AGN episode responsible for driving the outflows. As noted by Zubovas and Maskeliunas (2023), spatially resolved and/or multiphase observations are key to distinguishing fossil AGN outflows from star formation-driven ones, which may have similar integrated properties.

Table 4: Summary of fossil outflow candidate properties.

Object	Redshift	W_{80} [km s ⁻¹]	χ_1^2	χ_2^2	Key Signature
U4_13108_H	1.31	259	1.52	1.00	Broad non-Gaussian H α , lopsided
GS4_20422_K	2.00	—	1.64	1.61	Broad H α decoupled from [N II]
U4_34515_YJ	1.02	—	1.38	1.21	Red wing, widespread detections
COS4_06327_YJ	0.80	—	2.03	1.82	Broad component, lopsided to east
U4_29207_YJ	0.83	—	1.19	1.18	Bipolar: blue SW, red NE
COS4_17395_YJ	1.09	—	1.37	1.17	Persistent blue wing
U4_15499_YJ	0.92	305	1.76	1.39	Horizontal blue wing, perpendicular [N II]
COS4_15698_YJ	1.09	—	1.37	1.17	Horizontal W_{80} band through nucleus

6 Conclusion and Outlook

Future Use and a small comment on the future of Data representation in Astronomy

Lorem ipsum

A List of Acronyms

AGN	active galactic nuclei	ISM	Interstellar Medium
BLR	broad line region	KMOS	K-band Multi-Object Spectrograph
BPT	diagnostic based on the ratio of a high ionization line to a low one, named after Baldwin, Phillips and Terlevich	KMOS^{3D}	KMOS 3D Survey
EELR	Extended Emission Line Region	NLR	narrow line region
ENLR	Extended Narrow Line Region	SMBH	supermassive black hole
GUI	Graphical User Interface	SNR	Signal to noise ratio
IFU	Integral Field Unit	SPH	Smoothed Particle Hydrodynamics
IFS	Integral Field Spectroscopy	WHAN	diagnostic diagram based on the equivalent width of H α and the [N II]/H α ratio

B Acknowledgements

I would like to express my gratitude to my supervisor, Dr. Dominika Wylezalek, for her guidance and support throughout the course of this research. I would also like to thank Prof. Dr. Jochen Heidt for taking on the role of the second examiner in this thesis. In general, I would like to thank the entire Emmy Noether Research Group GALENA, for their support and help through this semester, especially Marco Albán for his invaluable contributions to the project, and for their helpful feedback and suggestions. I would also like to acknowledge the use of the following software and tools: Astropy, a community-developed core Python package and an ecosystem of tools and resources for astronomy, Topcat, which is a fast tool for editing and visualising FITS-Data, and L^AT_EX, which was a great help to me during writing this thesis. Furthermore, I would like to thank Marvin-SDSS for providing access to the MaNGA-Survey. Finally, I would like to thank my colleagues and friends for their encouragement and support throughout the course of this research and here too, I would like to highlight two names, namely Jan Küpperbusch and Maximilian Rieger, who accompanied and supported me throughout the bachelor's degree. This work would not have been possible without their help and support.

C Licences & Data

C.1 KMOS3D by (Wisnioski et al., 2019)

As discussed in @todo, the data used in this thesis originates from the KMOS^{3D} survey (Wisnioski2019). The KMOS^{3D} survey is made publicly available under the following link: <https://www.mpe.mpg.de/ir/KMOS3D/data>.

C.2 PyQT5

Many thanks to the developer of PyQT5 Martin Fitzpatrick. PyQT5 was used in this thesis to create the GUI for the emission line fitting, visualisation of stacked spectra and W80-histogram analysis.

C.3 Streamlink

Streamlink was used in this thesis for visualization of the fitted data and connection between my work and other cited sources. Streamlink is licenced under the following Apache License 2.0:

```
<!--
```

```
Copyright (c) Streamlit Inc. (2018-2022) Snowflake Inc. (2022-2025)
```

```
Licensed under the Apache License, Version 2.0 (the "License");  
you may not use this file except in compliance with the License.  
You may obtain a copy of the License at
```

```
http://www.apache.org/licenses/LICENSE-2.0
```

Unless required by applicable law or agreed to in writing, software distributed under the License is distributed on an "AS IS" BASIS, WITHOUT WARRANTIES OR CONDITIONS OF ANY KIND, either express or implied. See the License for the specific language governing permissions and limitations under the License.

-->

D References

- Antonucci, R. (1993). Unified models for active galactic nuclei and quasars. *Annual Review of Astronomy and Astrophysics*, *31*, 473–521.
- Baldwin, J. A., Phillips, M. M., & Terlevich, R. (1981). Classification parameters for the emission-line spectra of extragalactic objects. *PASP*, *93*, 5–19. <https://doi.org/10.1086/130766>
- Beckmann, V., & Shrader, C. (2012). *Active Galactic Nuclei*. Wiley-VCH.
- Belfiore, F., Maiolino, R., Maraston, C., Emsellem, E., Bershad, M. A., Masters, K. L., Yan, R., Bizyaev, D., Boquien, M., Brownstein, J. R., Bundy, K., Drory, N., Heckman, T. M., Law, D. R., Roman-Lopes, A., Pan, K., Stanghellini, L., Thomas, D., Weijmans, A.-M., & Westfall, K. B. (2016). SDSS IV MaNGA - spatially resolved diagnostic diagrams: a proof that many galaxies are LIERs. *Monthly Notices of the royal Astronomical Society*, *461*(3), 3111–3134. <https://doi.org/10.1093/mnras/stw1234>
- Binette, L., Magris, C. G., Stasińska, G., & Bruzual, A. G. (1994). Photoionization in elliptical galaxies by old stars. *AAP*, *292*, 13–19.
- Blandford, R. D., & Znajek, R. L. (1977). Electromagnetic extraction of energy from Kerr black holes. *Monthly Notices of the Royal Astronomical Society*, *179*, 433–456. <https://doi.org/10.1093/mnras/179.3.433>
- Cantiello, M., Jermyn, A. S., & Lin, D. N. C. (2021). Stellar evolution in AGN disks. *The Astrophysical Journal*, *910*, 94. <https://doi.org/10.3847/1538-4357/abdf4f>
- Cappellari, M., & Copin, Y. (2003). Adaptive spatial binning of integral-field spectroscopic data using Voronoi tessellations. *Monthly Notices of the Royal Astronomical Society*, *342*(2), 345–354. <https://doi.org/10.1046/j.1365-8711.2003.06541.x>
- Cid Fernandes, R., Stasińska, G., Mateus, A., & Vale Asari, N. (2011). A comprehensive classification of galaxies in the Sloan Digital Sky Survey: how to tell true from fake AGN? *Monthly Notices of the royal Astronomical Society*, *413*(3), 1687–1699. <https://doi.org/10.1111/j.1365-2966.2011.18244.x>
- Cid Fernandes, R., Stasińska, G., Schlickmann, M. S., Mateus, A., Vale Asari, N., Schoenell, W., & Sodré, L. (2010). Alternative diagnostic diagrams and the ‘forgotten’ population of weak line galaxies in the SDSS. *Monthly Notices of the royal Astronomical Society*, *403*(2), 1036–1053. <https://doi.org/10.1111/j.1365-2966.2009.16185.x>
- Dojčinović, I., Kovačević-Dojčinović, J., & Popović, L. Č. (2023). The flux ratio of the [n ii] lines in sample of active galactic nuclei type 2. *Advances in Space Research*, *71*, 1219–1226.
- Fabian, A. C. (2012). Observational Evidence of Active Galactic Nuclei Feedback. *Annual Review of Astronomy and Astrophysics*, *50*, 455–489.
- Ferrarese, L., & Merritt, D. (2000). A Fundamental Relation between Supermassive Black Holes and Their Host Galaxies. *The Astrophysical Journal*, *539*.
- Flesch, E. W. (2023). The million quasars (milliquas) catalogue, v8. *The Open Journal of Astrophysics*.
- Förster Schreiber, N. M., et al. (2019). The KMOS3D Survey: Demographics and Properties of Galactic Outflows at $z = 0.6$ - 2.7 . *The Astrophysical Journal*, *875*.
- Gebhardt, K., et al. (2000). A Relationship between Nuclear Black Hole Mass and Galaxy Velocity Dispersion. *The Astrophysical Journal*, *539*.

- Genzel, R., et al. (2014). Evidence for Wide-spread AGN-driven Outflows in the Most Massive $z \sim 1 - 2$ Star-forming Galaxies. *The Astrophysical Journal*, 796.
- Harrison, C. M., et al. (2014). Kiloparsec-scale outflows are prevalent among luminous AGN. *Monthly Notices of the Royal Astronomical Society*, 441.
- Harrison, C. M., et al. (2018). AGN outflows and feedback: twenty years on. *Nature Astronomy*, 2.
- Herpich, F. R., Stasińska, G., Cid Fernandes, R., Vale Asari, N., & Mateus, A. (2018). On the gas content and efficiency of AGN feedback in low-redshift quasars. *Monthly Notices of the royal Astronomical Society*, 473(4), 5211–5223. <https://doi.org/10.1093/mnras/stx2672>
- Hickox, R. C., & Alexander, D. M. (2018). Obscured Active Galactic Nuclei. *Annual Review of Astronomy and Astrophysics*, 56.
- Ho, L. C. (2008). Nuclear Activity in Nearby Galaxies. *ARA&A*, 46, 475–539. <https://doi.org/10.1146/annurev.astro.45.051806.110546>
- Hubble, E. P. (1926). Extragalactic nebulae. *The Astrophysical Journal*, 64.
- Kauffmann, G., Heckman, T. M., Tremonti, C., Brinchmann, J., Charlot, S., White, S. D. M., Ridgway, S. E., Brinkmann, J., Fukugita, M., Hall, P. B., Ivezić, Ž., Richards, G. T., & Schneider, D. P. (2003). The host galaxies of active galactic nuclei. *Monthly Notices of the royal Astronomical Society*, 346(4), 1055–1077. <https://doi.org/10.1111/j.1365-2966.2003.07154.x>
- Kellermann, K. I., et al. (1989). The radio-loud/radio-quiet dichotomy in quasars. *The Astronomical Journal*, 98.
- Kennicutt, J., Robert C. (1998). Star Formation in Galaxies Along the Hubble Sequence. *Annual Review of Astronomy and Astrophysics*, 36.
- Kewley, L. J., Dopita, M. A., Sutherland, R. S., Heisler, C. A., & Trevena, J. (2001). Theoretical Modeling of Starburst Galaxies. *Astrophysical Journal*, 556(1), 121–140. <https://doi.org/10.1086/321545>
- Kewley, L. J., Groves, B., Kauffmann, G., & Heckman, T. (2006). The host galaxies and classification of active galactic nuclei. *Monthly Notices of the royal Astronomical Society*, 372(3), 961–976. <https://doi.org/10.1111/j.1365-2966.2006.10859.x>
- King, A., & Pounds, K. (2015). Powerful Outflows and Feedback from Active Galactic Nuclei. *Annual Review of Astronomy and Astrophysics*, 53.
- King, A. R., et al. (2011). Fossil outflows from active galactic nuclei. *Monthly Notices of the Royal Astronomical Society: Letters*, 415.
- Kormendy, J., & Ho, L. C. (2013). Coevolution (Or Not) of Supermassive Black Holes and Host Galaxies. *Annual Review of Astronomy and Astrophysics*, 51.
- Lemaître, G., & Rowan-Robinson, M. (2001). *The nine numbers of the cosmos*. Oxford University Press.
- Lopes, A. R. et al. (2025). The s-plus fornax project (s+fp): Mapping $h\alpha+[n\text{ ii}]$ emission. *A&A*, 699.
- Madau, P., & Dickinson, M. (2014). Cosmic Star-Formation History. *Annual Review of Astronomy and Astrophysics*, 52.
- Mahatma, V. H., et al. (2018). Remnant radio-loud AGN in the Herschel-ATLAS field. *Monthly Notices of the Royal Astronomical Society*, 475.

- Netzer, H. (2013). *The Physics and Evolution of Active Galactic Nuclei*. Cambridge University Press.
- Netzer, H. (2015). Revisiting the Unified Model of Active Galactic Nuclei. *Annual Review of Astronomy and Astrophysics*, 53.
- Osterbrock, D. E., & Ferland, G. J. (2006). *Astrophysics of Gaseous Nebulae and Active Galactic Nuclei* (2nd). University Science Books.
- Padovani, P., et al. (2017). Active galactic nuclei: what's in a name? *The Astronomy and Astrophysics Review*, 25.
- Peterson, B. M. (2006). The Broad-Line Region in Active Galactic Nuclei. *Physics of Active Galactic Nuclei at all Scales*.
- Schneider, P. (2015). *Extragalactic Astronomy and Cosmology: An Introduction* (2nd). Springer.
- Shakura, N. I., & Sunyaev, R. A. (1973). Black holes in binary systems. Observational appearance. *Astronomy and Astrophysics*, 24.
- Silk, J., & Rees, M. J. (1998). Quasars and galaxy formation. *Astronomy and Astrophysics*, 331, L1–L4.
- Stasińska, G., Cid Fernandes, R., Mateus, A., Sodr e, L., & Asari, N. V. (2006). Semi-empirical analysis of Sloan Digital Sky Survey galaxies - III. How to distinguish AGN hosts. *Monthly Notices of the royal Astronomical Society*, 371(2), 972–982. <https://doi.org/10.1111/j.1365-2966.2006.10732.x>
- Stasińska, G., Vale Asari, N., Cid Fernandes, R., Gomes, J. M., Schlickmann, M., Mateus, A., Schoenell, W., & Sodr e, L., Jr. (2008). Can retired galaxies mimic active galaxies? Clues from the Sloan Digital Sky Survey. *Monthly Notices of the royal Astronomical Society*, 391(1), L29–L33. <https://doi.org/10.1111/j.1745-3933.2008.00550.x>
- Stockton, A., & MacKenty, J. W. (1984). The extended giant-branch and planetary-nebula populations. *The Astrophysical Journal*, 283.
- Tadhunter, C. N., et al. (1987). The extended narrow-line region in radio galaxies. *Nature*, 325.
- Thorne, J. (2021). *AgN unification diagram*. Retrieved January 11, 2026, from <https://zenodo.org/records/6381013>
- Urry, C. M., & Padovani, P. (1995). Unified Schemes for Active Galactic Nuclei. *Publications of the Astronomical Society of the Pacific*, 107.
- van Dokkum, P., Brammer, G., Momcheva, I., Skelton, R. E., & Whitaker, K. E. (2013). 3d-hst data release v3.0: Extremely deep spectra in the udf and wfc3 mosaics in the 3d-hst/candels fields. <https://arxiv.org/abs/1305.2140>
- Volonteri, M. (2010). Formation of Supermassive Black Holes. *The Astronomy and Astrophysics Review*, 18.
- Wisnioski, E., et al. (2015). The KMOS3D Survey: Design, First Results. *The Astrophysical Journal*, 799.
- Wisnioski, E., et al. (2019). The KMOS^{3D} Survey: Data Release and Final Survey Paper. *Astrophysical Journal*, 886.
- Zakamska, N. L., & Greene, J. E. (2014). Quasar feedback and the physics of the interstellar medium. *Monthly Notices of the Royal Astronomical Society*, 442.
- Zubovas, K. (2018). AGN outflow duty cycle and the M–sigma relation. *Monthly Notices of the Royal Astronomical Society*, 473.

- Zubovas, K., Bialopetravičius, J., & Kazlauskaite, M. (2022). Intermittent AGN episodes drive outflows with a large spread of observable loading factors. *Monthly Notices of the Royal Astronomical Society*, 514(2), 1705–1719. <https://doi.org/10.1093/mnras/stac1274>
- Zubovas, K., & King, A. (2012). Clearing out a galaxy. *The Astrophysical Journal*, 745.
- Zubovas, K., & Maskeliunas, G. (2023). Life after AGN switch off: evolution and properties of fossil galactic outflows. *Monthly Notices of the Royal Astronomical Society*, 524(4), 4819–4840. <https://doi.org/10.1093/mnras/stad1661>

E Statutory Declaration

I hereby declare that I have written this thesis independently and have used only the sources and aids indicated. Literally quoted sentences or parts of sentences are marked as such; other references in terms of content and scope are indicated by full details of the publications concerned. The work in the same or similar form has not yet been submitted to and published by any examination authority. This work has also not yet been used in any form in another examination or as performance in a course.

Heidelberg, 1 January 2026

Signature:

Ich erkläre hiermit, dass ich die vorliegende Arbeit selbstständig verfasst habe und dabei ausschließlich die angegebenen Quellen und Hilfsmittel verwendet habe. Wörtlich zitierte Sätze oder Teile von Sätzen sind als solche gekennzeichnet; andere Bezüge in Bezug auf den Inhalt und Umfang sind durch vollständige Angaben der betreffenden Veröffentlichungen gekennzeichnet. Die Arbeit in gleicher oder ähnlicher Form wurde noch keiner Prüfungsbehörde vorgelegt und veröffentlicht. Diese Arbeit wurde bisher auch nicht in irgendeiner Form in einer anderen Prüfung oder als Leistung in einem Kurs verwendet.

Heidelberg den 01. Januar 2026

Unterschrift: